Chapter 10 -- Power and Particle Handling and First Wall

10.1 Introduction and General Considerations

Over the past two decades it has been demonstrated that control of neutrals- and impurity influx is a prerequisite for enhanced plasma performance in tokamaks. More recently, it has been shown that this is also true for stellarators [1,2]. Accordingly, the NCSX program has incorporated a strong plasma boundary component from the very start of the design. This is accomplished by implementing heat removal and particle- and impurity control through thoughtful design of the plasma-facing components (PFCs) on the one hand and the control of plasma-wall interactions on the other hand.

Due to their three-dimensional topology, stellarators don't necessarily have the ordered magnetic field line structure outside the separatrix found in axisymmetric tokamaks. Hence, plasma-facing components matched to the plasma surface, also must be three-dimensional. Depending on the configuration, PFCs can function as limiters or divertors. In a magnetic configuration with a separatrix, we define the plasma-facing component to be a "limiter" if it is located inside the last closed magnetic surface (LCMS) and intercepts closed field lines, thereby defining the plasma boundary. The same PFC can be a "divertor plate" if it is outside the LCMS and intercepts open field lines only. A fixed set of PFCs can function as divertor plates or limiters by magnetically changing the plasma configuration.

A limiter has the advantage of defining the last closed surface and can thus simplify the boundary structure by cutting off islands and ergodic regions, but the disadvantage is that it is in direct contact with the confined plasma and, hence, can be a strong source of recycling neutrals and impurities. A divertor, on the other hand, provides the advantage of an interface between the plasma and the solid wall which is removed from the confined plasma and buffered by the divertor plasma. However, in a stellarator, the boundary of the main plasma can be very complex, with islands and ergodic regions with short connection lengths which can themselves interact locally with the walls. Therefore, limiter operation may be more easily controllable for initial plasma operation.

The PFC design in NCSX is carried out with the goal to minimize the impact on plasma performance in the following sense: 1). Heat removal has to be accomplished in a way which avoids excess temperatures on the material surfaces. 2) Neutrals from recycling have to be controlled internally (baffles) and/or externally (pumps) to minimize effects on plasma performance. 3) The plasma-surface interaction has to be designed for minimum impurity generation.

The first and most basic task of the boundary program is the study of the field line structure outside the LCMS. This is the basis for the design of limiter- or divertor plates and, to some degree, the vacuum vessel. In a modular stellarator, such as NCSX, the plasma configuration outside the separatrix can be very complicated and detailed studies are needed, supported by modeling and experiment, before the optimum divertor can be designed. Some of the basic features can be adopted from the experience of W7-AS and the design studies for W7-X. The

Wendelstein group has studied an approach for a stellarator divertor for more than a decade [3] and has developed modeling tools [4] as well as carried out divertor experiments [5]. The final phase of the Wendelstein divertor development is an island divertor in which the islands outside the LCMS are intercepted by divertor plates (open field lines) and the particles are pumped by cryo-pumps located behind baffles. Although the NCSX configuration is different from the Wendelstein configuration, Poincaré plots indicate that field lines outside the LCMS accumulate in the top and bottom of the bean-shaped cross sections and divertor baffles should be effective for neutrals control in these locations.

Since more modeling work and experimental experience is necessary before the ultimate divertor can be designed, we plan a phased approach for the NCSX boundary and divertor development. In the first phase the emphasis is on flexibility to accomodate different plasma configurations and this initial phase might not be optimal concerning all required functions. Adequate power handling, of course, is a prerequisite. The subsequent development will be based on further modeling, experimental feed back and model validation and will eventual lead to the final version combining optimized heat removal with good neutrals- and impurity control.

10.2 Magnetic Topology Outside the Last Closed Magnetic Surface

As indicated above, stellarators are generally lacking the ordered magnetic field line structure with nested surfaces found in the scrape-off layer of axisymmetric devices. For the M45 coil set of NCSX, the field lines do not form nested surfaces outside the LCMS, but make many toroidal revolutions close to it. Especially the field-lines launched within 1 cm outside of the LCMS don't exhibit very strong stochasticity. This is shown in Figure 10-1 which depicts Poincaré plots for planes with the toroidal angles of 0, 30, 60, and 90 degrees.

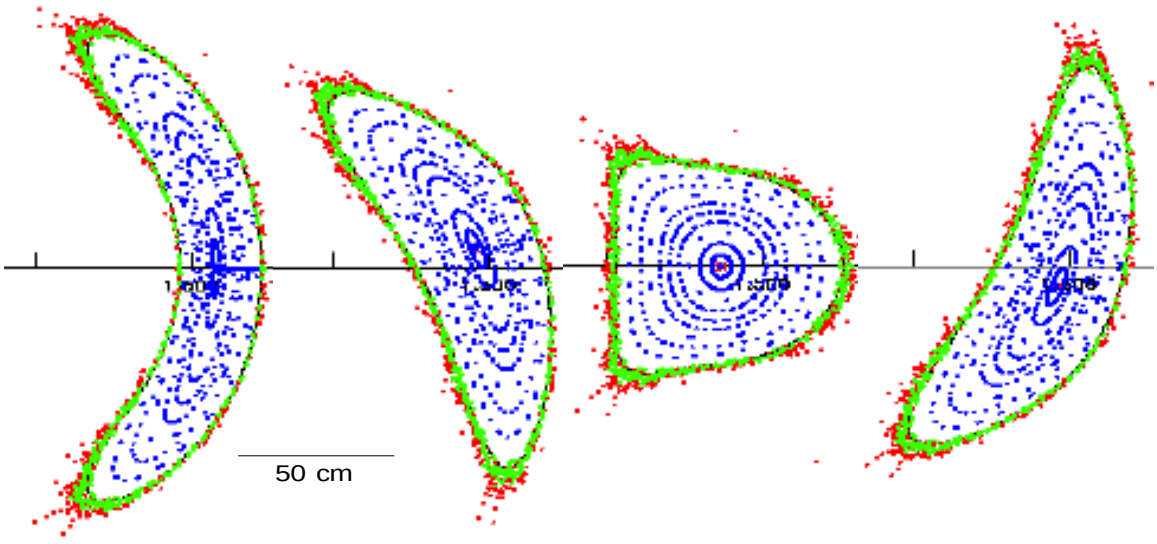

Figure 10-1. Poincaré plots for field-line intersections at poloidal cross-sections of 0, 30, 60, and 90 degrees; launched at outside midplane (green) and inside midplane (red), followed for 20 toroidal revolutions.

The Poincaré plots in Figure 10-1 are generated by following 10 field-lines launched at the outboard midplane (green) and 10 field-lines launched at the inboard midplane (red) for 20 toroidal revolutions; the plots represent the full-current, full-beta case. Typical Kolmogorov lengths L_k for field-lines shown in Figure 10-1 are shorter than the connection lengths, namely in the order of 50 m, while the field-lines were followed for 20 revolutions, or approximately $L_c \sim$ 180 m. So, we find that L_k is smaller than L_c, which means the field-lines are somewhat but not strongly stochastic ($L_k << L_c$). When field-lines are launched further out of the LCMS, the stochasticity increases, as indicated in the Poincaré plot in Figure 10-2 which compares plots for field-lines launched between 0 and 1 cm versus between 0 and 4 cm respectively.

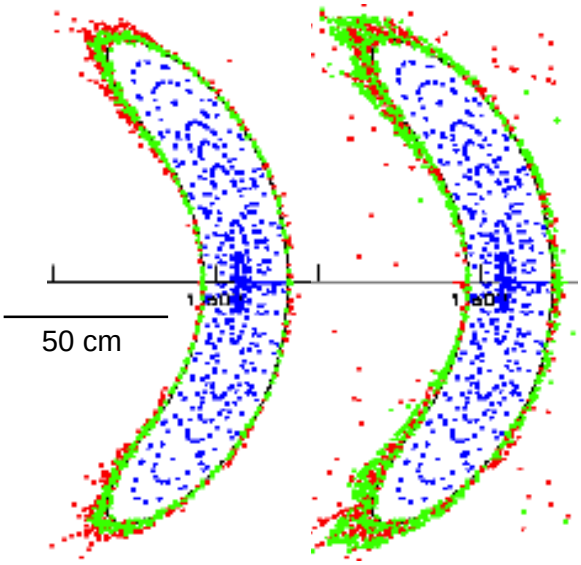

Figure 10-2. Poincaré plots at f=0 plane for field-lines launched between 0 and 1 cm (left) and for field-lines launched between 0 and 4 cm, at inside (red) and outside (green) midplane

For practical reasons, individual features of the boundary layer need to be considered for vacuum vessel and PFC design, with the goals of small angles of incidence of field lines and large wetted areas to distribute power loads uniformly. The diversion properties of the field-lines can be seen especially in the bean-shaped cross section (ϕ=0): between the midplane and the top and bottom of the bean-shape, the field-lines diverge by a factor >5, which helps to spread out heat- and particle fluxes. For this reason, these areas are suited as locations for divertor structures. Finally, some degree of configurational flexibility is required, so the particle and heat loads are adequately handled even with changes in the core plasma configuration such as rotational transform, shear, beta, etc.

In this study we make extensive use of a code originally developed for the design of the divertor of the W7-X stellarator, Magnetic Field Solver for Finite Beta Equilibria (MFBE), which is a new magnetic topology code developed by E. Strumberger [6], for magnetic configurations which have finite plasma pressure. Prior calculations for W7-X used vacuum magnetic fields outside LCMS. As in those calculations, vacuum magnetic fields are calculated exactly from given coil currents by the Biot-Savart law. In addition to vacuum fields, MFBE calculates all magnetic fields of finite-beta free boundary equilibria with plasma currents on a

grid whose nodes may be arbitrarily close to the plasma boundary. Unlike other stellarators, QAS configurations have a bootstrap current comparable to a tokamak with the same iota, with NCSX having an external transform fraction in the range of 60-80%. The presently used version of MFBE is modified from the version used previously [6], by treating equilibria with toroidal current via the virtual casing principle of Shafranov-Zakharov [7].

For the plasma boundary studies, the VMEC2000 code described in Section 3.1 is used to determine free boundary finite beta NCSX equilibria. The VMEC2000 code is an energy minimizing equilibrium code which assumes nested flux surfaces and therefore cannot be used to study islands and stochastic regions inside the LCMS. The PIES code described in Section 3.3 and HINT free boundary codes are able to treat islands and stochastic regions, but do not provide this information outside the LCMS. Coupling of the VMEC2000 and MFBE codes allows the LCMS to be found by an iteration procedure involving the toroidal flux parameter, PHIEDGE. The MFBE code obtains as input the Fourier coefficients of potential (at the boundary), flux surfaces and magnetic field from the free boundary VMEC2000. To obtain high numerical accuracy in the calculation of magnetic fields near the LCMS, the number of integration points is adaptive in the distance from the plasma boundary.

10.3 Significance of the SOL connection lengths

10.3.1 Introduction

The connection length, L_c, of field lines in the SOL outside the last closed magnetic surface (LCMS) is an important parameter which determines the temperature profile of the SOL plasma along the field lines. Long connection lengths allow high separatrix temperatures and significant temperature drops along field lines to reasonably low target temperatures, and hence the establishment of a high recycling regime with a low impurity source at the target. If L_c is too short, the temperature profile along the field lines could be very flat with moderate to low temperature at both the target and separatrix. This could result in poor core confinement due to low edge temperature and possibly thermal instabilities at the edge due to impurity radiation cooling. Field line tracing (see Figure 10-1) indicates that one key to insuring long SOL field line length is to allow a sufficient gap between the LCMS and the material boundary, especially at the tips of the bean-shaped cross sections.

The plasma temperature at the target surface will determine the recycling regime and impurity source rate from sputtering. The temperature upstream at the LCMS is the boundary condition for the core temperature profile. Tokamak experience has shown that this separatrix temperature sets the height of the pedestal at the edge of the core plasma. Since the temperature profiles are stiff inside the tokamak core plasma, this means that the core energy content and confinement can be very sensitive to the separatrix temperature. This may also be the case in a compact, nearly axisymmetric stellarator like NCSX.

The purpose of this section is to present the implications of either short or long connection length on SOL temperatures (separatrix and target) and thereby raise awareness of the possible effect these two conditions could have on core confinement, impurity source and neutral

hydrogen source. The analysis is most easily accomplished with the 2-point divertor model which connects the upstream temperature and density with the corresponding divertor parameters [8,9].

10.3.2 Two-point divertor model

The principal assumptions of the 2-point model are as follows: particle balance is achieved on each flux tube individually, the only sink for ions is at the divertor plate and each resulting neutral is re-ionized in a thin layer above the plate, balancing the losses. The pressure balance between upstream separatrix ("sep") and divertor ("div") is given by the equation $n_{sep}T_{sep}(1+M_{sep}^2) = n_{div}T_{div}(1+M_{div}^2)$, where the upstream Mach number is $M_{sep}=0$ and the divertor Mach number is $M_{div}=1$, i.e. the pressure balance is simply $n_{sep}T_{sep} = 2n_{div}T_{div}$. The power balance along the field lines (s-coordinate) is

$$\frac{d}{ds}\left(\kappa \cdot \frac{dT}{ds}\right) = \frac{P_{sol}}{A_{sol} \cdot L_c} \qquad (10\text{-}1)$$

where $\kappa = \kappa_0 T^{5/2}$ is the parallel thermal conductivity, with $\kappa_0 = 31000/(Z_{eff} ln\Lambda)$, and P_{sol} and A_{sol} are the power into the SOL and the area of the SOL perpendicular to the power flux respectively. Assuming that the right-hand side of this equation is independent of s, the power balance can be integrated twice and yields

$$T_{sep}^{7/2} - T_{div}^{7/2} = \frac{7}{2}\frac{q_{//}L_c}{\kappa_0} \qquad (10\text{-}2)$$

with $q_{//} = P_{sol}/A_{sol}$. Finally, $q_{//}$ and the divertor parameters are linked by the sheath condition: $q_{//} = \gamma n_{div} T_{div} c_s$ with $\gamma \sim 7$ the sheath heat transmission coefficient and c_s the sound speed at the divertor. Thus we have three equations to link the upstream parameters with the divertor parameters:

$$n_{sep}T_{sep} = 2n_{div}T_{div} \qquad (10\text{-}3)$$

$$T_{sep}^{7/2} - T_{div}^{7/2} = \frac{7}{2}\frac{q_{//}L_c}{\kappa_0} \qquad (10\text{-}4)$$

$$q_{//} = \gamma\, n_{div}T_{div}c_s. \qquad (10\text{-}5)$$

Since input power and upstream density are usually the plasma control parameters, they are the input parameters here and all other needed parameters are determined with equations (10-3) to (10-5).

For estimating the NCSX target and upstream temperatures we use $Z_{eff} = 1.5$ and make the following assumptions:
total power: $P_0 = 3$ MW, 6 MW
core radiatio fraction: $f = 0.2$
power into the SOL: $P_{sol} = P_0(1-f) = 2.4$ MW , 4.8 MW

SOL power scale length: $\lambda q\perp = 0.02$ m
effective major and minor radii: $R_{eff} = 1.42$ m, $a_{eff} = 0.33$ m
Asol = $4\pi R\, \lambda q\perp (B_\theta/B)$ (extra factor of 2 accounts for two ends); $(B_\theta/B) \sim 0.13$ for $iota_{edge} \sim 0.65$.
Our main interest is to determine the temperature difference between the upstream (separatrix) location and the divertor as a function of connection length and upstream density and power. This is illustrated in Figures 10-3 and 10-4

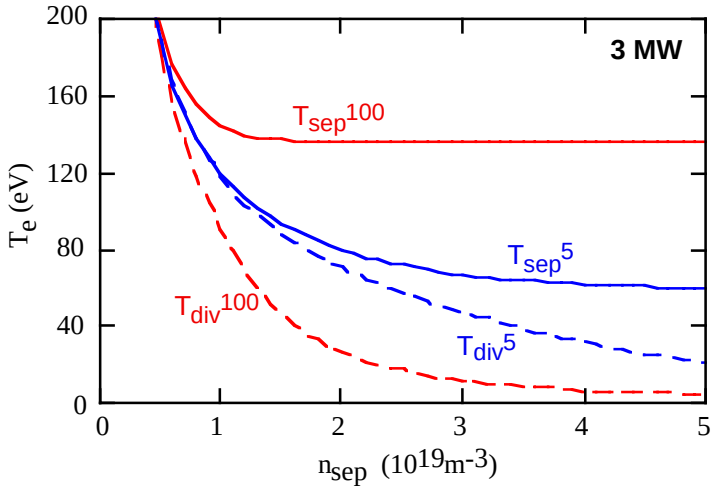

Figure 10-3. Separatrix and divertor temperatures for L_c = 5 m and L_c = 100 m as a function of separatrix density n_{sep}, for P = 3 MW input power.

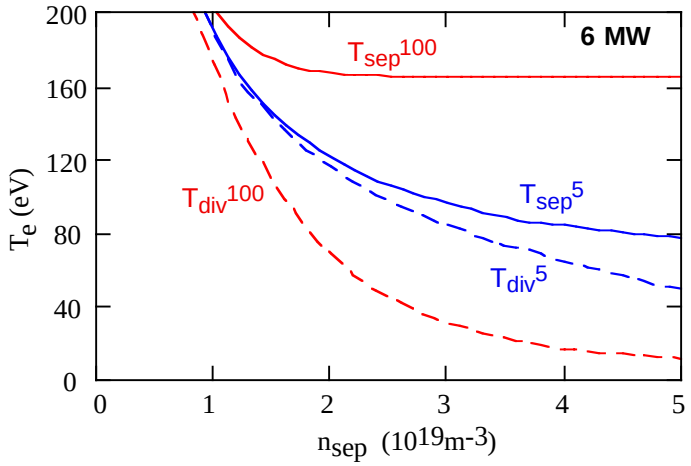

Figure 10-4. Separatrix and divertor temperatures for L_c = 5 m and L_c = 100 m as a function of separatrix density n_{sep}, for P = 6 MW input power.

To demonstrate the connection length effect, we have compared a short connection length of L_c = 5 m with a long connection length of L_c = 100 m. Field line tracing indicates that connection lengths in excess of 100 m should be achievable in NCSX for > 80% of the field-lines launched between 0-1cm at the outside and inside midplane. To achieve low target sputtering and a high recycling regime in tokamaks one usually tries to minimize the plasma temperature near the targets while keeping the plasma from detaching. This means to keep T_{div} in the range of 10-20 eV. From Figure 10-3 this low target temperature is reached in a deuterium plasma for the short

L_c case only at the lower input power, $P_{inj} \sim 3$ MW and high densities; the upstream temperature will be about 60 eV. Higher input power raises the upstream temperature but the target temperature also increases. For the 6 MW case in NCSX the separatrix and target temperatures are getting very close to each other. At low separatrix density ($3x10^{19}$ m^{-3}) the target temperature is much too high for considerations of plate sputtering and at higher separatrix density ($5x10^{19}$ m^{-3}) the separatrix temperature is too low for good core confinement (see sections below).

Long connection lengths, $L_c \sim 100$ m, allows substantial temperature drop in the SOL flux tube as shown in Figures 10-3 and 10-4. At the higher input power of 6 MW, solutions with $T_{div} \sim 10$ eV and $T_{sep} \sim 160$ eV are possible at a separatrix density of $5x10^{19}$ m^{-3} (Figure 10-4). Even at lower density, $3x10^{19}$ m^{-3}, solutions with $T_{div} \sim 30$ eV and $T_{sep} \sim 160$ eV are possible with 6 MW of input power.

10.3.3 Implications of short vs. long connection length

A separatrix temperature in the 40 eV range with carbon impurities can lead to thermal instability. The carbon cooling curve increases sharply with decreasing T_e from 40 eV down to about 7 eV (see Figure 10-5).

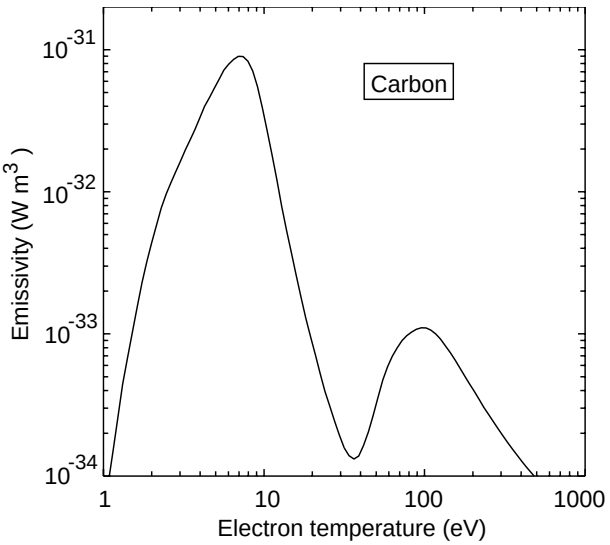

Figure 10-5. Carbon emissivity (ε) vs. electron temperature showing emissivity increase with decreasing temperature in the range $7 < T_e < 40$ eV; radiated power is $\varepsilon n_e n_c$

If this instability occurs around the LCMS, the expected result is a high density, low temperature mantle which is strongly radiating at the edge of the core plasma. If the temperature profile of the core plasma is stiff, as it is in tokamaks, then low separatrix temperature will produce low core confinement. In diverted tokamaks the effect of this carbon thermal instability is observed in experiments with heavy gas injection to high density [10]. As the density in the SOL increases the temperature drops and the carbon radiation in the SOL increases somewhat with no appreciable decrease in core confinement. However, when the temperature at the separatrix is reduced to about 40 eV, the carbon radiation is observed to move rapidly inside the separatrix and the core confinement is reduced by a factor of two.

Long connection length allows a substantial temperature difference to be established between upstream separatrix temperature and target temperature. The separatrix temperature can be consistent with good core confinement while at the same time the target temperature can be consistent with low physical sputtering of carbon targets. The physical sputtering curve for deuterium on carbon is given in Ref. 9, p. 119. For the long L_c solution at $P_{inj} = 6$ MW and $n_{sep} = 5x10^{19}m^{-3}$, $T_{div} \sim 10$ eV and the carbon sputtering is a factor of three less than would be the case with short L_c and $T_{div} \sim 40$-60 eV.

Another advantage of long connection lengths is that most of the temperature drop occurs near the target so the core plasma is screened from incoming neutrals by ionization in the hot plasma not far from the target. This leads to high recycling conditions near the target at moderate core density and it can even lead to detachment and substantial reduction of the heat flux on the target at higher core density. Strong temperature gradients near the target can lead to transport of impurities away from the targets by the ∇T_i force. However the high recycling solution typically also generates sufficient flow toward the targets that the drag force on impurities balances the ∇T_i force and impurities are reasonably well entrained near the target surface. Shaping of structures in the vicinity of the targets can help to entrain the impurities.

10.3.4 Conclusions

Applying the two-point model of 1D energy transport in the SOL has shown that for NCSX parameters a connection length of order 5 m is insufficient to produce the desired high separatrix temperature and low target temperature needed for good core confinement and low target impurity sputtering. A connection length of order 100 m or larger would be sufficient to produce the needed large temperature drops along SOL flux tubes from the separatrix to the target. Long connection lengths for a sufficiently large number of field lines should be achievable in the NCSX design. In particular, field line tracing calculations indicate that extension of the boundary farther away for the LCMS in the top and bottom of the bean-shaped regions should produce the desired connection length.

10.4 Phased Plasma-Facing Component Development

The vacuum vessel will be made of stainless steel and the initial plasma-facing components will be made of graphite. The ideal case would be to cover the whole first wall with graphite which would take care of neutral beam shine-through, energetic particle losses, and limiter/divertor baffles all together. But, this ideal case would be expensive and is also not needed for the initial phase of machine operation with an input power of 3 MW for 0.3 s.

The magnetic field configuration of the plasma boundary in NCSX is three-dimensional and stochastic. For this reason, the design of the plasma-facing components is not straight-forward and needs a phased approach, generating the needed design information through iteration between modeling and experimental observation. Ideally, each phase of the development should build on the previous one.

Phase 1: 1st plasma and shakedown
Machine shake-down of all systems. There is no power deposition on the vacuum vessel walls and no plasma-facing components required. However, the initial simple limiter system to protect the walls will be in place at this point.

Phase 2: Vacuum and field-line mapping
This is the vacuum phase in which the magnetic flux surfaces will be mapped with an electron beam. This is mainly a check of the coils. Since there will be no significant power to any of the vacuum vessel parts, specific PFCs are not needed during this phase. Since the vacuum magnetic surfaces are substantially different from the finite beta case, measuring the vacuum flux surfaces is of very limited use for the design of the PFCs.

Phase 3: Ohmic operation
In the Ohmic phase the flux surfaces are not in their final configuration, since the current distribution is not similar enough to the bootstrap current at finite beta. But several hundred kilowatts of Ohmic power (100-300 kW) need to be removed from the vessel and this will require some simple graphite limiters for wall protection.

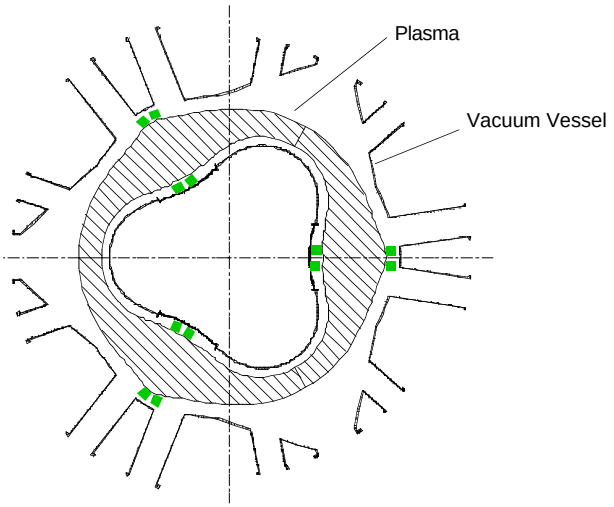

Figure 10-6. Plan view of the plasma and vacuum vessel. The figure shows (in green) the three initial limiters (one for each field period)

Phase 4: Auxiliary heating
The auxiliary heating phase with injection of initially 3 MW and later 6 MW of neutral beam power will require graphite coverage of the areas of beam shine-through, direct orbit losses, and the locations of thermal power and particle fluxes. This phase will allow first useful measurements of particle and power fluxes to the walls including finite beta effects on the shape of the flux surfaces and the plasma boundary. This will provide the detailed information for the design of the divertor capable of particle control and up to 6 MW of input power.

Phase 5: Confinement and beta limits
During this phase confinement and beta limits will be explored. This phase will include neutral beam injection of 6 MW and a divertor configuration with full power and particle handling

capability. Particle control in support of high plasma performance will be an essential requirement in this phase.

Phase 6: Long-pulse operation

Long-pulse operation will require (1) active particle control through divertor pumping and (2) long-pulse heat removal, possibly with active cooling of the divertor plates, depending on the pulse length. (cf. Figure 10-8)

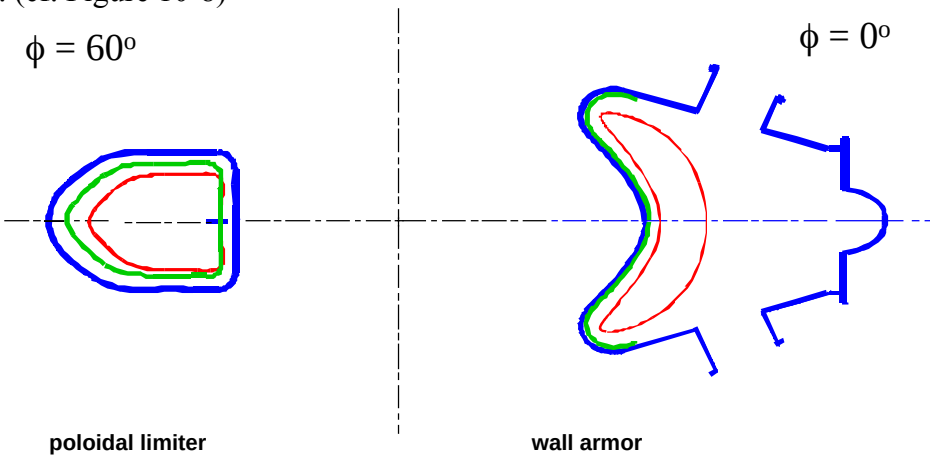

Figure 10-7. Plasma (red) and vacuum vessel cross-section (blue) at the ϕ = 0° (right) and ϕ = 60° (left) cross-sections. The left-hand side shows the approximate shape of one of the poloidal limiters (green), while the right-hand side shows the conformal wall armor (green) for auxiliary heating and initial divertor operation.

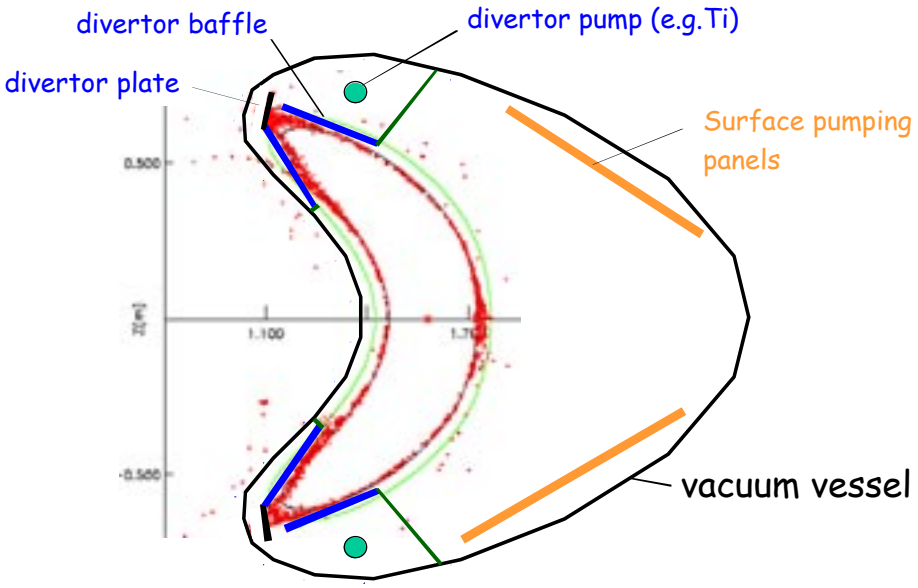

Figure 10-8. Divertor configuration including neutrals baffles with pumping slot and Ti-sublimators; also shown are possible surface pumping panels (with Li, Ti, or other) for additional recycling control.

10.5 Initial Estimates of Wall Heat Flux from Field-Line Tracing

Since the power loads on the wall depend largely on the specific design of the PFC configuration, we calculate here more generally typical peaking factors that can be expected from the characteristic stripes resulting from the plasma contacting the wall. As an example, we have chosen the $\phi = 60^{o}$ cross-section by moving the wall as close as 2 cm to the plasma to investigate the resulting peaking factors. Similar calculations will be done for the loads on the actual PFCs.

The results of the field-line tracing can be used to estimate the power loading on the wall surfaces. Here we describe the calculation of the relative distribution of intersecting field lines on the wall versus toroidal and poloidal angles, including the effects of cross-field diffusion. The data for the wall intersections are taken from the field-line tracing calculations using the GOURDON code by Koniges, Grossman et al. [11], following the work of Strumberger and Kisslinger [12-16].

The wall for these calculations is taken as a surface that is nearly conformal to the VMEC LCMS, but then shifted outward in major radius, such that the minimum gap on the inner wall is 2 cm , while on the outer wall, the gap is ~10 cm. This geometry is shown in Figure 10-9 at the "bullet" cross-section. Because of the outward shift of the wall, virtually all of the field-line intersections occur on the inside. The coordinates used are the toroidal angle, ϕ, which has its origin (=0) at the center of the bean cross-section, and the poloidal angle, θ, with its origin on the inner midplane of the cross-section. The bullet cross-section shown in Figure 10-9 corresponds to $\phi=60^{o}$. The field-lines are begun at the red triangles and subsequent intersections with the $\phi=60^{o}$ surface are shown in yellow. Here the field-lines diffuse in the perpendicular direction with a diffusion coefficient of 1 m^2 /s to simulate anomalous cross-field heat diffusion. The wall is shown as the outer line in blue.

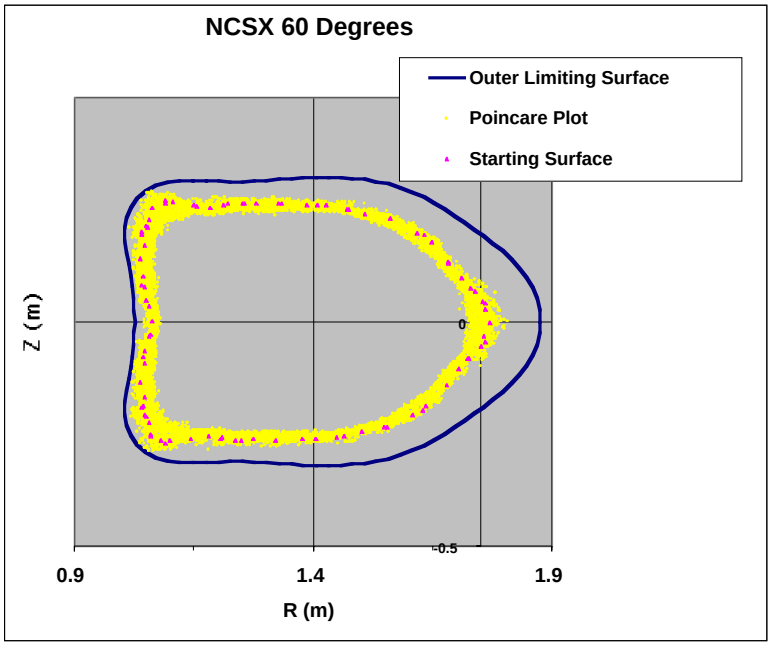

Figure 10-9. Starting surface points shown as red triangles superimposed on a Poincaré surface plot (yellow). The position of the limiting surface is given by blue curve.

The intersections with the wall are shown in Figure 10-10. There are no intersections found for $|\theta| > 90^o$, and there is toroidal periodicity every 120 ^{o}. Note that there is some fine-scale structure in the toroidal and poloidal directions that can be explained based on the piecewise representation of the wall and the finite step-size of the field-line integration. The wall is represented by plates having 100 poloidal segments and 24 toroidal segments in one field period (120^o toroidally). The GOURDON calculation also provides the angle with which the field-lines intersect the wall; this data is partially influenced by the piecewise representation of the wall.

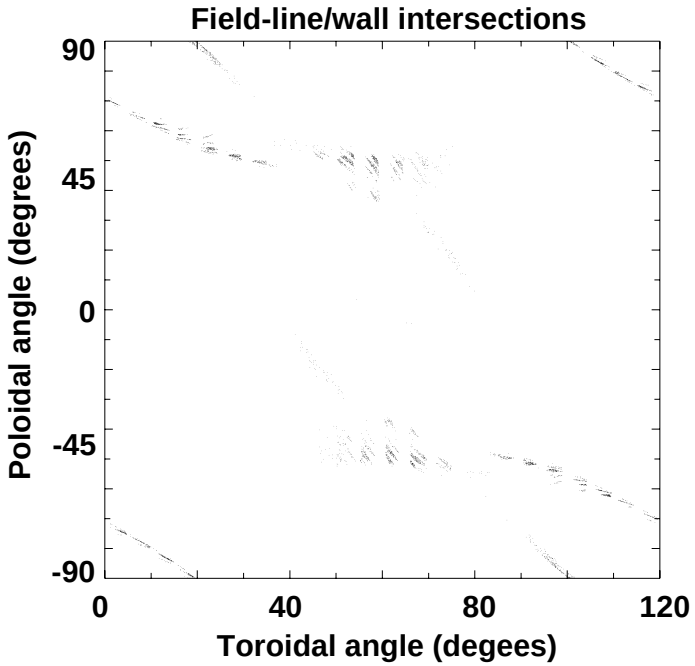

Figure 10-10. Field-line intersections with the outwardly shifted wall for NCSX. The (toroidal, poloidal) angles of (ϕ,θ) = (0,0) correspond to the inner midplane of the bean-shaped flux surface.

In order to estimate the heat flux to the wall, we have produced a numerical distribution function of the field line intersection. We bin the data on a uniform 2D mesh in (ϕ,θ) space using linear interpolation. It is necessary to optimize the size of the mesh, in that one too fine over-emphasizes that fine-scale structure arising form the piecewise representation of the wall and the finite integration step, while too coarse a representation artificially broadens the distribution. The results of two different mesh sizes is shown in Figures 10-11 and 10-12, where we have normalized the distribution such that it represents the increase over a uniform distribution of field-line intersections. The two mesh sizes are (25,50) and (50,50) for the (ϕ,θ) coordinates. The dark blue background corresponds to any value of the peaking factor less than unity.

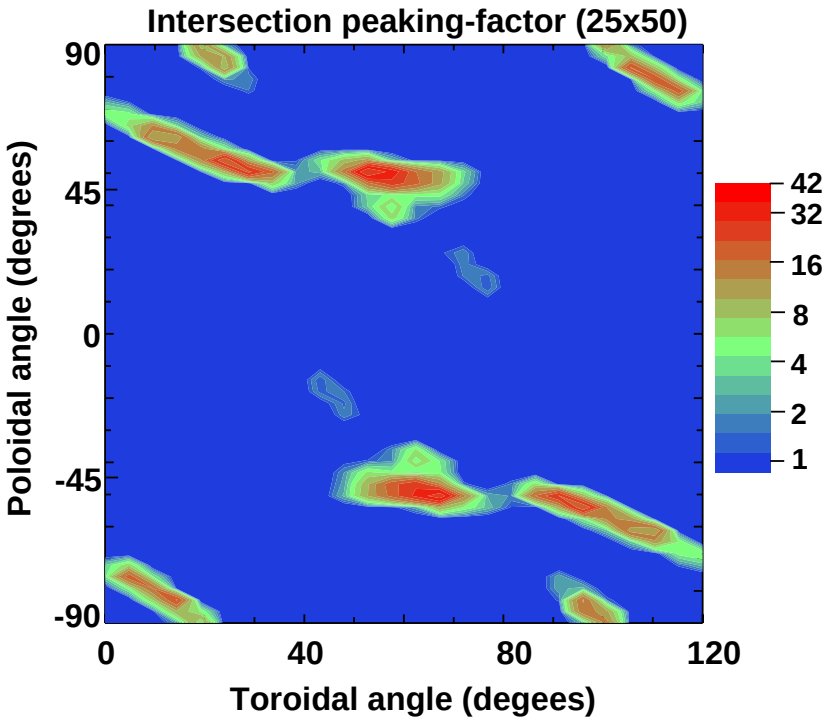

Figure 10-11. Density of field-line intersections on the wall normalized to a uniform distribution for a (ϕ,θ) mesh of (25,50) showing a maximum peaking factor of 42, assuming $D_{\wedge} = 1\ m^2/s$.

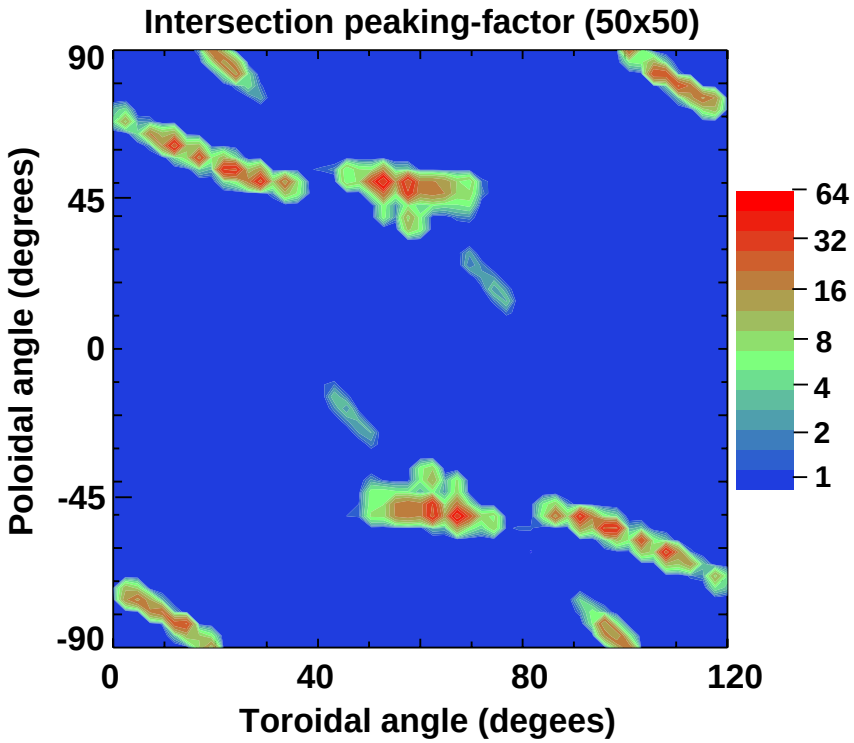

Figure 10-12. Distribution of field-line intersections for a (ϕ,θ) mesh of (50x50) giving a maximum peaking factor of 62, assuming $D_{\wedge} = 1\ m^2/s$.

Note that for the (50x50) case, the toroidal structure from the piecewise wall is beginning to show quite strongly as isolated red diamonds. A similar test was done by using a (25x100) mesh, but there the structure in the poloidal direction begins to be apparent, but the maximum peaking factor is 51, only a modest increase form the maximum of 42 for the (25,50) case. Thus, the (25x50) mesh appears to be close to the best to represent the distribution of field-line intersections that does not over-emphasize the piecewise nature of the model. This case predicts a maximum peaking factor of about 40, such that the maximum power load, S_{max}, would be given by

$$S_{max} = 40 \times P_{wall} / A, \qquad (10\text{-}6)$$

where P_{wall} is the power to the wall, and A is the first-wall surface area, which is approximately 40 m^2, i.e. a total wall power of e.g. 6 MW would result in a power flux of 6 MW/m^2 . Note that we have ignored the nonlinear variation of the surface area with the toroidal and poloidal angles. We could fold this information into the estimate, but much of the power comes in the "bullet" cross-section, where the geometry is not too distorted from a cylinder, as opposed to the strongly shaped bean section. The effect of a range of intersection angles is to broaden the power profile some. Since the strongest B-field is in the toroidal direction, we expect this incremental broadening to occur predominantly in this toroidal direction where the profile is already rather broad such that a large change would not be expected.

10.6 Neutrals Modeling

10.6.1 Monte-Carlo Neutrals Transport Modeling

The transport of neutral hydrogen atoms and molecules from various plasma facing surfaces into the scrape-off layer (SOL) and core plasma is studied with the DEGAS neutral transport code. Although fully three-dimensional (3D) simulations of neutral particle transport in NCSX are in preparation, the following discussion is limited to two-dimensional (2D) calculations in toroidal and cylindrical geometry. The primary objective of these studies is to examine core plasma fueling and power loss issues in non-axisymmetric stellarator geometry. Particular attention is focused on neutral penetration of the radially thin region near toroidal angle ϕ=0.

The plasma shape, specified in terms of a "moments" representation for R and Z, was obtained via a VMEC equilibrium for the PVR reference case case. Although this is not the final configuration, the neutrals considerations don't change significantly. Toroidally axisymmetric simulations are done using poloidal cross section shapes from a variety of toroidal angles. Effects of the 3D geometry are captured in calculations for several poloidal cuts combined with a midplane cut in cylindrical geometry (assuming direction normal to the torus midplane is ignorable). In the core plasma region of closed VMEC flux surfaces, the DEGAS grid is computed using a subset of those surfaces. In the region outside the last closed flux surface (LCFS), the grid is generated by constructing closed surfaces that are approximately conformal to the LCFS. (Flux expansion in the SOL near the tips of the "bean" cross sections is ignored.) The radial extent of the SOL grid surfaces is taken to be poloidally constant at 7.4 cm, which is roughly the minimum distance from the LCFS to the vacuum vessel wall for the PVR reference

case equilibrium. The "halo" region between the last SOL grid surface and the wall is assumed to contain no plasma.

The plasma profiles used in these calculations (see Figure 10-13) are analytic approximations to those constructed as described in section 7.3, and an assessment of the W7-AS experimental database for the edge and SOL conditions [17]. The electron and ion temperatures are assumed to be equal. The SOL parameters are characterized by exponential decay lengths. For "reference" plasma conditions shown in Figure 10-13 the density and temperature decay lengths are 2 cm and 3 cm, respectively. In order to test the sensitivity of the core fueling and ion charge-exchange power loss to the SOL plasma, simulations are also performed for a "thin" SOL with density and temperature decay lengths that are 1/2 of the reference values. In these calculations the core and LCFS

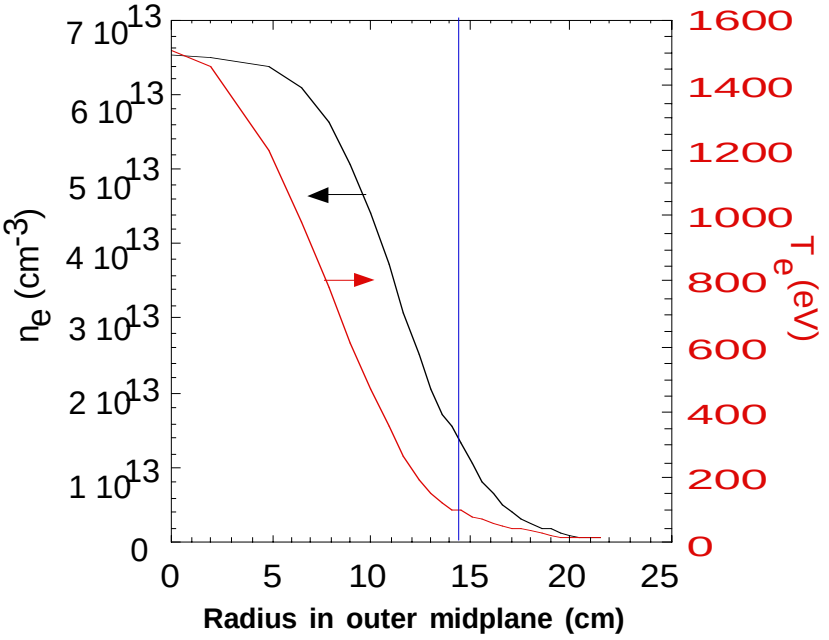

Figure 10-13. Density and temperature profiles for the reference background plasma used in the 2-D DEGAS calculations are based on the neoclassical transport analysis of Section 7.3. The radius is measured along the outboard midplane of the $\phi = 0$ poloidal cut.

plasma parameters, as well as the assumed recycling ion flux, are held fixed. The plasma parameters shown in Figure 10-13 are referenced to the radius in the outboard midplane in the $\phi = 0$ "bean" cross section. In order to isolate the effects of the 3-D geometry and the location of the recycling surfaces, the density and temperature are held fixed in the poloidal and toroidal directions within each flux tube (or SOL grid tube) .

The assumed locations of the plasma facing surfaces and plasma recycling surfaces are shown in Figure 10-14 for the $\phi = 0$ poloidal cross section. Also shown are the LCFS and the last grid surface defining the SOL. Toroidally axisymmetric simulations for the $\phi = 0$ cross section are performed (1) with only the vacuum vessel and the vertical target plates present, (2) with the baffles added and (3) with all of the components present. Calculations for the $\phi = 30$ and $\phi = 60$ degree cross sections include only the vacuum vessel and target plates.

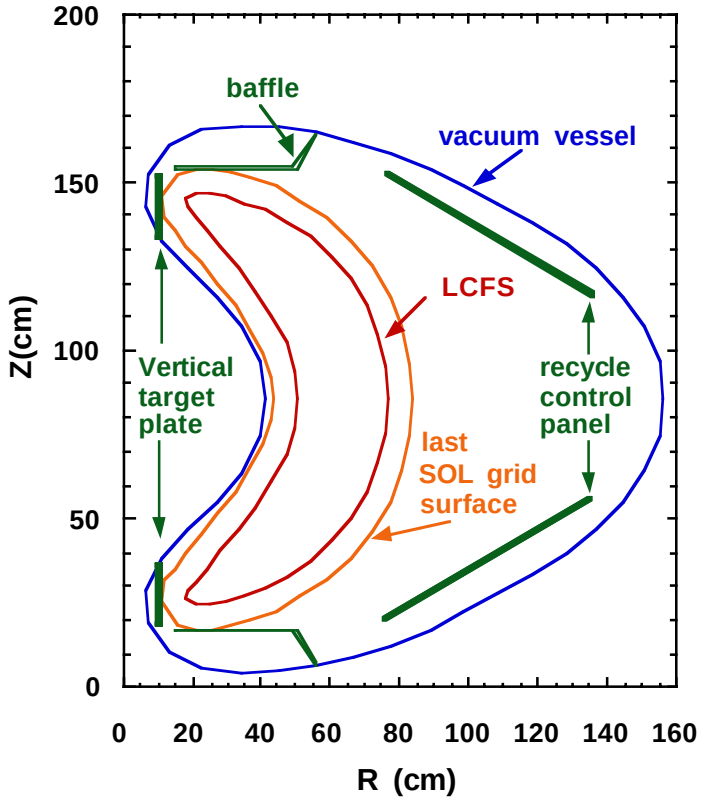

Figure 10-14. Plasma facing surfaces and plasma recycling surfaces used in neutral transport simulations are shown in the $\phi = 0$ poloidal plane.

Since the SOL grid surfaces have been constructed as closed surfaces rather than open surfaces terminating on the target plates, we simulate the recycling process with gas puffs from the plates. The average energy of ions striking the plate $\langle E_i \rangle$ is calculated from the averages of T_e and T_i across the SOL and the assumed sheath potential (3 T_e) . For the reference plasma parameters $\langle E_i \rangle$=165 eV. The particle reflection coefficient for carbon is taken to be 0.22 and the average reflected energy to be 60 eV for this average ion impact energy. The gas puffs that simulate ion recycling are then composed of 22% atomic species at a temperature of 40 eV and 78% molecular at the assumed plate or wall temperature. In addition it is assumed that the integrated ion recycling flux at each of the two plate or wall segments in each simulation is 1000 amps (1 amp = 6.25×10^{18} ions/s). The neutral source at each plate or wall segment is then 1.36×10^{21} atoms/s and 2.44×10^{21} molecules/s. It is emphasized that this neutral source is *assumed* and

without neutral-neutral interactions the calculated neutrals quantities scale directly with the recycling flux. The corresponding particle confinement time, leading to the assumed particle flux, would be ~ 4 ms, which is smaller than one would assume for the core particle confinement time , because it takes into account local recycling at the plates.

Quantitative results of the 2-D neutrals penetration calculations and their dependence on flux surface geometry and recycling location are here presented as 1-D radial, 1-D poloidal, and 1-D toroidal distributions. The 1-D radial profiles are poloidally averaged, whereas the poloidal and toroidal distributions are plotted for the radius corresponding to the flux tube just inside the last closed magnetic surface.

Radial distributions of atomic neutral density for the $\phi = 0$ and the $\phi = 60$ degree cross sections are shown in Figure 10-15. Two recycling locations are chosen for comparison: the divertor target plates, and the vacuum vessel wall segments at the inboard midplane. Since the width of the SOL and the plasma parameters within each of the SOL grid tubes are poloidally constant, the poloidally averaged neutral atomic density in the SOL shows only a weak dependence on recycling location.

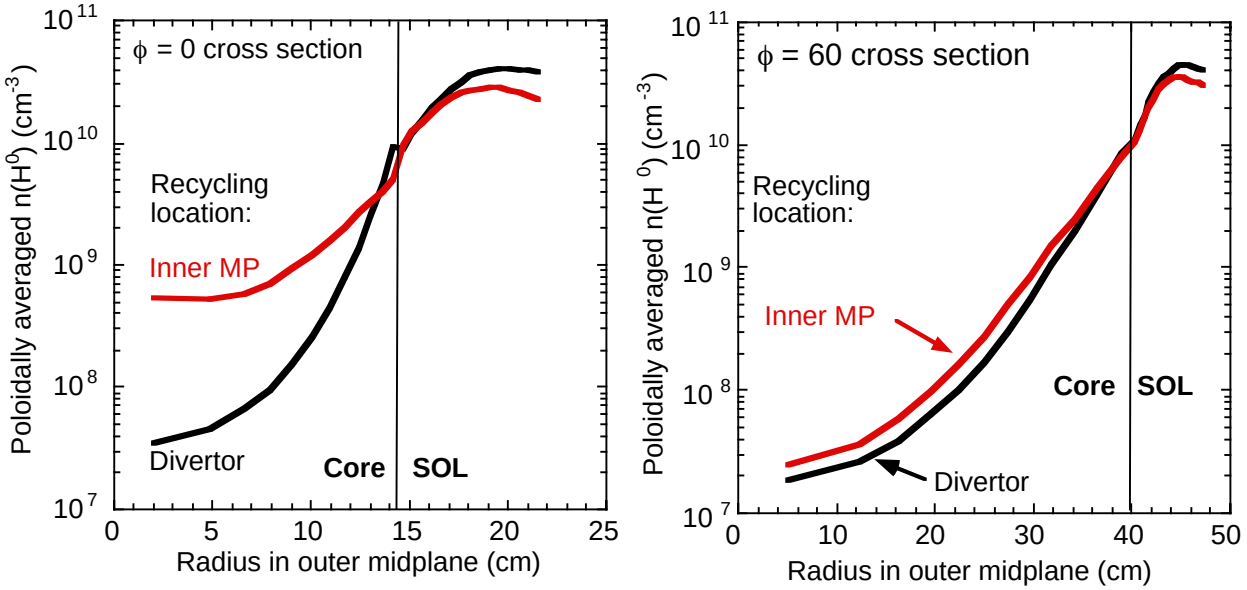

Figure 10-15. Poloidally averaged atomic neutral density distributions in the $\phi = 0$ cross section simulation show a strong dependence on the poloidal location of the recycling surface. Those for $\phi = 60$ show little dependence and those for $\phi = 30$ (not shown) are intermediate between the $\phi = 0$ and 60 curves.

For the same reasons and because of the shape of the flux surfaces, the neutral density profiles in the core plasma of the $\phi = 60$ degree ("bullet" cross section) case also show little dependence upon recycling location. The $\phi = 0$ simulations shows that the neutral density profile in the core plasma depends strongly upon the radial thickness of the core plasma as "seen" by the recycling neutrals and the cross section presented by the core flux surfaces to the neutral flux from the recycling surface.

Poloidal distributions of atomic neutral density just inside the separatrix, presented in Figure 10-16 for the ϕ =0 case, show the expected dependence upon recycling location. The width of the angular distribution for outer midplane recycling is twice that for inner midplane recycling for the reasons discussed above. The narrowness of the distribution for the case of divertor plate recycling is partly due to the narrow "bean" tip and partly due to the definition of poloidal angle (origin at the minor axis) for the flux surface shape.

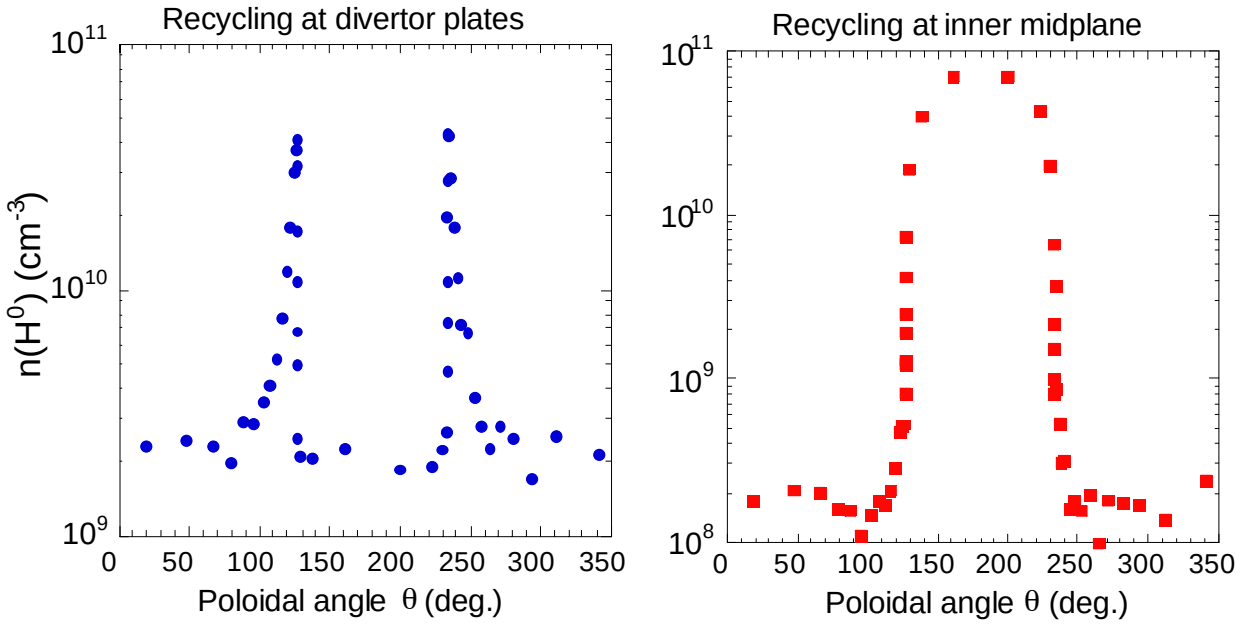

Figure 10-16. Poloidal distributions of atomic neutral density just inside the separatrix for ϕ = 0 simulations with two recycling locations.

The effects of flux surface geometry and recycling location on core fueling rates and core ion power loss are focal issues for this study. For the reference plasma parameters the calculated core fueling rates are 15-20% of the integrated recycling flux for the axisymmetric ϕ =0, 30, and 60 degree cross section simulations. The corresponding core ion power loss is 50-60 kW. If the recycling location is at the inner midplane of the vacuum vessel, the core fueling rate is 26-30% of the integrated recycling flux and the core ion power loss is 100-250 kW.

Simulations in which the density and temperature SOL decay lengths were reduced by 50% from the reference plasma values were done for the toroidally axisymmetric ϕ = 0 geometry. The largest effect of the thinner SOL is seen for recycling at the bean tips (see Figure 10-14), in which case the core fueling (core charge-exchange power loss) increased by 50% (65%). With midplane recycling the total ion power loss in the core is 20% higher than that for the reference

plasma and the core fueling rates are 26% higher for recycling from the inner midplane; the corresponding core fueling rate is 40% of the integrated recycling flux and the core ion power loss is 300 kW (120 kW).

Two possible methods for particle or recycling control have been briefly examined in this study. The first involves judicious placement of baffles near the "bean" tips to house cryo-pumps and collect neutrals (see Figure 10-14). The second relies upon pumping at recycle control panels in the space outboard of each of the "bean" cross sections. Although active pumping inside the baffles was not included, the baffle molecular pressure was calculated to be 0.25 mTorr for the reference plasma conditions and recycling at the divertor plates. The presence of the baffles also reduced the outboard midplane pressure by a factor of four when compared to the case with no baffles. An additional factor of almost four reduction in midplane pressure was obtained by placing panels as shown in Figure 10-14. Pumping by the panels is simulated with a sticking coefficient of 0.5 for both atoms and molecules.

Toroidal transport of neutrals from one field period to the next is seen in Figure 10-17 to be minimal for the SOL plasma parameters assumed here. For recycling at the $\phi = 0$ outboard midplane the neutral atomic density decreases by about a factor of 10 within 1/2 field period. Due to the much closer proximity of the strongly ionizing SOL plasma and the vacuum vessel wall at the $\phi = 60$ ("bullet") location, the neutral density decreases by a factor of 40 within 1/2 field period. For the midplane simulations presented in Figure 10-17 the recycling flux has been adjusted to give the same atomic neutral density in the midplane "halo" grid cells as that calculated in the corresponding $\phi = 0$ or 60 degree poloidal cross section cases. Due to reduced SOL ionization with the "thin" SOL plasma parameters, the decrease in the neutral density at a distance of 1/2 field period from the recycle location is slightly less than that for the reference plasma.

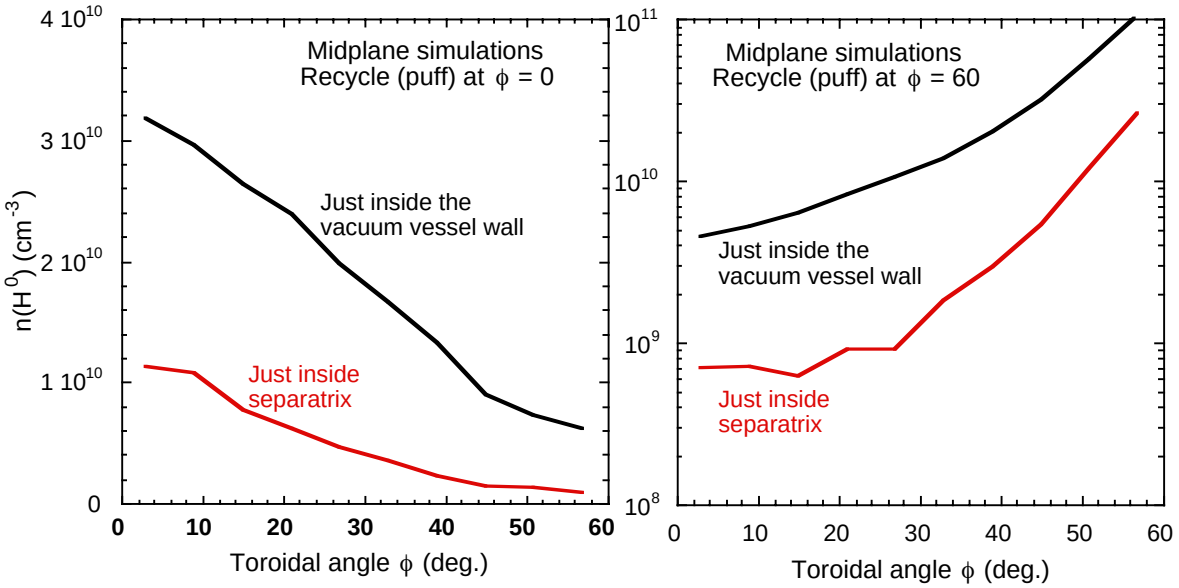

Figure 10-17. For the reference background plasma the atomic neutral density decreases by a factor of 10 (40) in the toroidal direction within 1/2 field period for recycling near the ϕ = 0 (60) outboard midplane.

10.6.2 Fluid neutrals modeling

Introduction

The 3D BoRiS code is being developed at IPP Greifswald in partnership with the Lawrence Livermore National Laboratory as a comprehensive numerical tool for modeling of edge plasmas in 3D geometry, in particular in stellarators. We have implemented a fluid neutrals model in BoRiS, which moves it towards becoming a full plasma-neutrals model potentially applicable to a variety of boundary plasma problems. In the present progress report we describe the application of the fluid neutrals model in BoRiS to the proposed NCSX stellarator. In these calculations the plasma is fixed and the geometry closely follows the NCSX geometry as given by the magnetic field data.

Physics model

The fluid neutrals description in BoRiS closely follows the models previously implemented in the tokamak edge code UEDGE. The neutral fluid consists of atoms with temperature equal to the ion temperature. For this fluid we solve the neutral density equation and the neutral momentum equation. The neutral density equation is

$$\frac{\partial}{\partial t}(n_N) + \nabla \cdot (n_N \vec{V}_N) = -S_i + S_r \qquad (10\text{-}7)$$

where S_i, S_r stand for the ionization and recombination sources.

For the neutral parallel momentum equation there are two options: the full Navier-Stokes equation and a simple diffusive model. The Navier-Stokes equation is

$$\frac{\partial}{\partial t}(mn_N V_{\|N}) + \nabla\cdot(mnV_N V_{\|N} - \eta_N \nabla V_{\|N}) = -\nabla_{\|} p_N + m_i n_i n_N K_{cx}(V_{\|i} - V_{\|N}) + m_i S_r V_{\|i} - m_i S_i V_{\|N}. \quad (10\text{-}8)$$

The diffusive approximation for the parallel velocity is

$$V_{\|N} = -D_N(\nabla_{\|} n_N / n_N + \nabla_{\|} T_N / T_N) + V_{\|i} \quad (10\text{-}9)$$

which corresponds to neglecting all but two terms in the Navier-Stokes equation. And the perpendicular neutral velocity is always calculated in the diffusive approximation

$$V_{\perp N} = -D_N(\nabla_{\perp} n_N / n_N + \nabla_{\perp} T_N / T_N) + V_{\perp i}. \quad (10\text{-}10)$$

In the diffusive model there is flux limiting in the form

$$j_N \rightarrow \frac{j_N}{[1 + a(\frac{j_N}{0.25 n V_{Ti}})^2]^{1/2}}. \quad (10\text{-}11)$$

The Navier-Stokes neutrals model in BoRiS has not, as yet, been sufficiently tested, while the diffusive model has been successfully benchmarked against UEDGE in 1D and 2D. Thus, presently we show calculations for NCSX done with the diffusive neutrals model.

Magnetic geometry

The geometry is based on the magnetic field calculated with the MFBE code [6]. We use a case which corresponds to an early configuration of NCSX, with $<R_{maj}> \cong 1.7$ m. For calculations in the NCSX reduced design geometry $<R_{maj}> \cong 1.4$ m, a uniform scaling factor 0.82 is applied.

The geometry is represented in magnetic [Boozer] coordinates normalized to unity. A mapping between the real coordinates R, Z, Φ_g and the magnetic coordinates s, θ, ϕ has been calculated using line tracing algorithms by our colleagues from IPP Greifswald. Then we used a Fourier expansion of this mapping to construct our simplified model of NCSX dimensions of NCSX flux geometry, which provides a good qualitative and quantitative match to the shape and flux tubes.

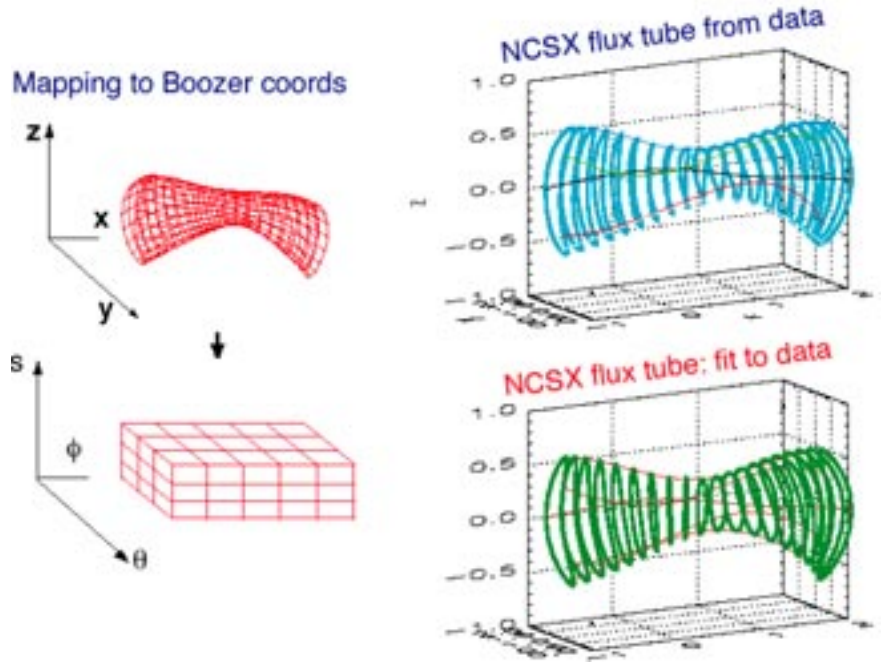

Figure 10-18. 3D view of NCSX flux tubes from the data and in the reduced model

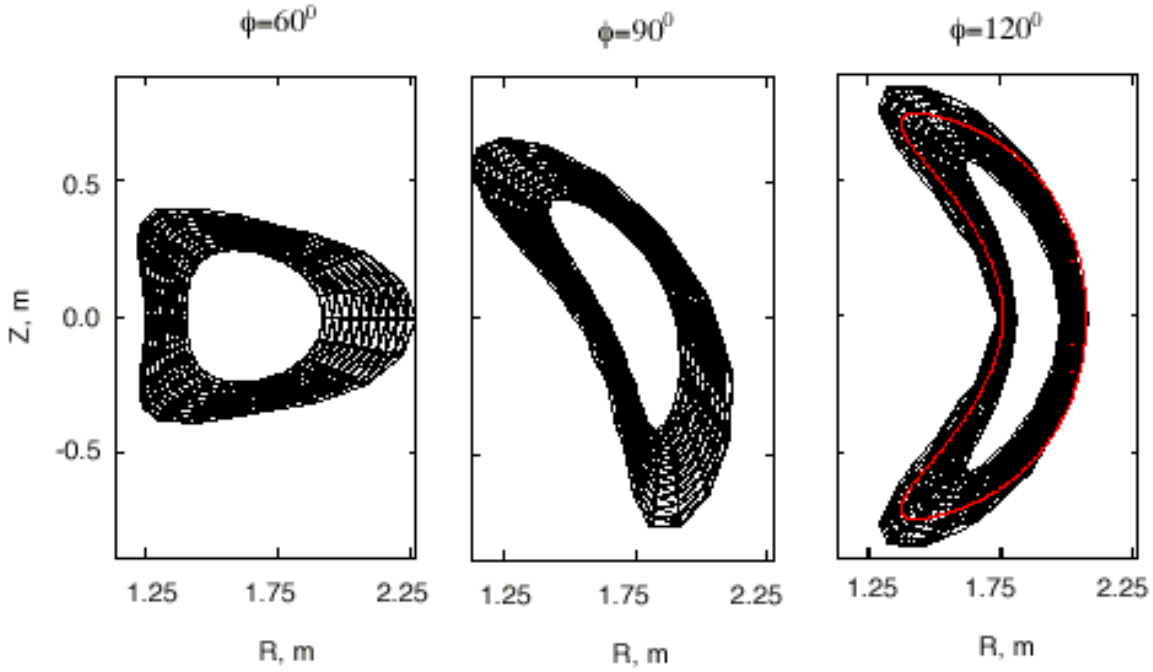

Figure 10-19. Three different cross-sections of the flux tubes by toroidal planes Φ_g = const.

The grid represents the BoRiS computational mesh. The computational cells are quadrilaterals but they are shown split into two or more triangles, which improves the smoothness of the graphical results. The radial coordinate has a range of $0 \le s \le 1$ with $s=2/3$, corresponding to the LCMS, so the inner 2/3 of the domain is inside the LCMS and outer 1/3 is

outside. For comparison, the LCMS from the MFBE code is shown on Figure 10-19 by the red line.

Boundary conditions

On the inner boundary of the domain **s** = 0 a zero neutral flux condition is set since very few neutral particles are supposed to get that far into the plasma. The outer boundary (**s** = 1) has also a zero flux condition which represents a perfect wall, except for an area $0.4 \le \theta, \varphi \le 0.6$ where a fixed neutral density $n_N = 10^{18}$ m^{-3} is set. This models a source of neutral gas localized at the inner mid-plane part of the "bullet" cross-section. This choice of boundary conditions is relevant to the proposed design of inboard limiters to be built on the inner side of the "bullet" cross-sections (see Figure 10-20) for the Ohmic phase (Phase 3).

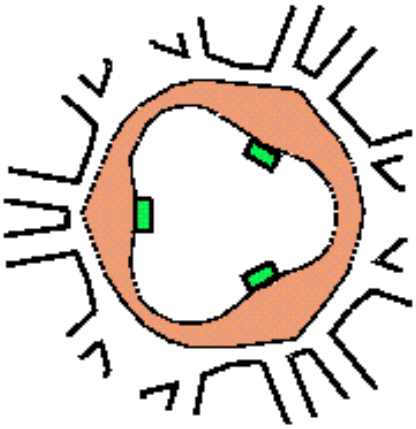

Figure 10-20 Boundary conditions used in BoRiS calculations of the gas density; the green squares represent inboard limiters (one for each field period).

Background plasma

For the background plasma we consider temperature and density profiles, which are dependent on the s coordinate only. The normalized profiles T/T_0, n/n_0 are taken in the form

$$[2-(3s/2)^2], \qquad 0 \le s \le 2/3$$
$$\exp(2-3s), \qquad 2/3 \le s \le 1$$

where the normalization parameters T_o, n_o are the LCMS values (see Figure 10-16).

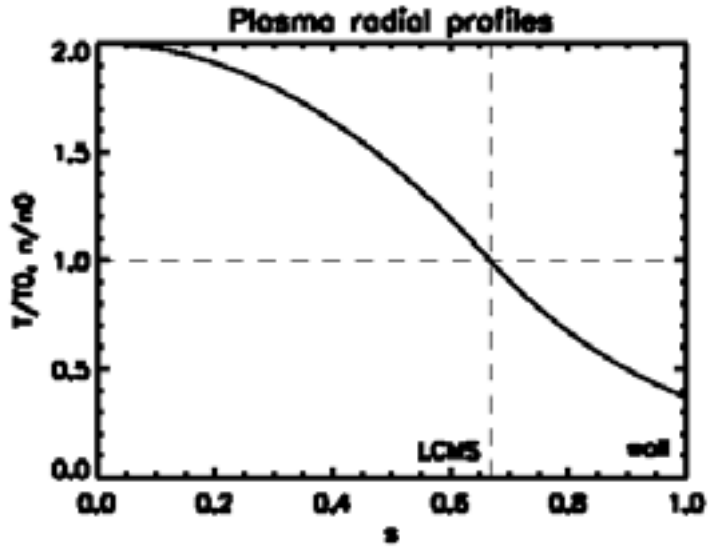

Figure 10-21. Normalized profiles for plasma density and temperature used for fluid neutrals modeling

Numerical results

For an example calculation we took T_0 as 50 eV and n_0 as $1x10^{19}$ m^{-3}. The distribution of neutral gas density is shown in Figure 10-22 for three toroidal cross-sections.

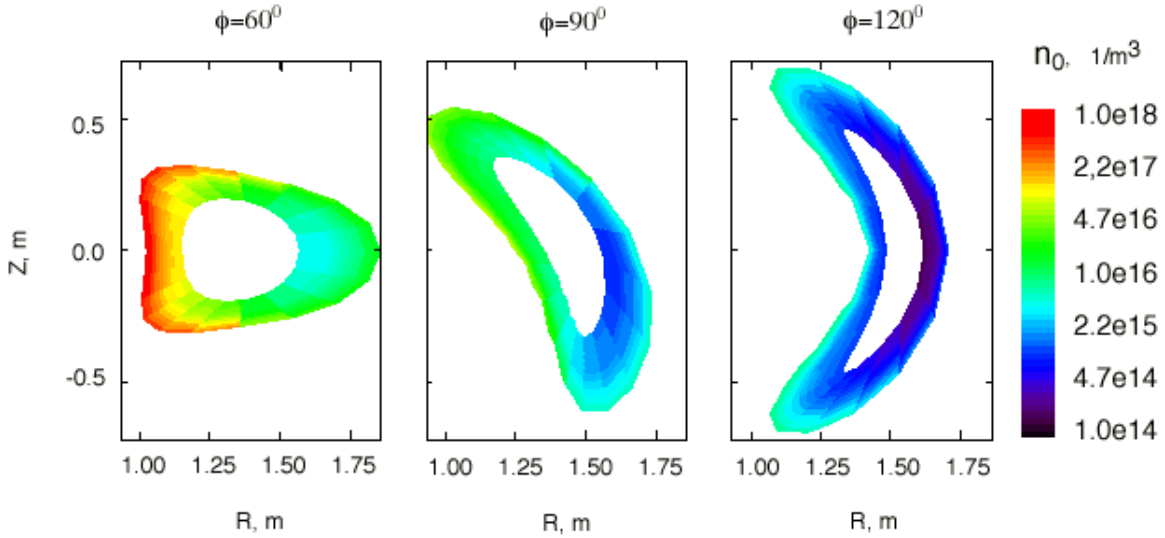

Figure 10-22. Neutrals distributions in NCSX from the BoRiS code with inboard limiter at the ϕ = 60 degree section

One can see some interesting features such as significant neutral penetration inside the LCMS, especially in the "bullet" cross-section; in the intermediate cross-section ($\varphi=90^0$) the neutrals are mainly in the upper-inner part; and in the "bean" cross-section the neutral density is quite small.

Conclusions

The neutrals fluid model which has been added to the BoRiS code at LLNL is capable of performing neutrals transport calculations in the 3D geometry of a stellarator. The BoRiS code can become a valuable numerical tool for modeling of a variety of edge plasmas in 3D. The present example was carried out at too low plasma density to be comparable with the 2D DEGAS results. In the future, the fluid neutrals model will be benchmarked with 2D DEGAS results.

10.7 Edge Plasma Modeling

10.7.1 Self-Consistent Edge-Plasma Transport Modeling

Estimating high heat-flux locations and magnitudes on the vessel wall via magnetic field-line tracing is described earlier, including diffusion to model turbulent cross-field thermal transport. While these are important tools to indicate where to place protective tiles on the walls, experience with tokamaks shows that a more complete transport model of the edge plasma, including particle, momentum, and energy flows, is needed to understand the variations that are possible for the heat-flux profiles, and for the particle fueling that is related to the core density limit. The interaction between the plasma and neutrals is the key issue here. Such a model will contribute to decisions about upgrades to the NCSX power and particle handling hardware including the most effective location of baffles to control fueling. A self-consistent model will provide vital information on the type and position of edge-plasma diagnostics, and is also needed to predict the level of impurities that can enter the core.

We have an active collaboration with IPP Greifswald to develop a 3D plasma/neutral fluid transport code called BoRiS. As part of this collaboration, we have worked with IPP to construct an initial computational mesh for the BoRiS 3D fluid code calculations for NCSX, which are utilized in the 3D fluid neutral modeling described above. We have now progressed to the point of solving the plasma transport equations for density, parallel momentum, and separate ion and electron temperatures in 3D, but most of our recent focus has been in benchmarking BoRiS in 2D with the UEDGE transport code. We will also include the plasma and neutrals together to obtain self-consistent edge-plasma profiles with respect to recycling. The detailed results of the 2D benchmarking and the 3D results will be presented at the PSI meeting in Gifu, Japan in May, 2002.

10.7.2 Edge-Plasma Turbulence Modeling

A very important component of the edge-plasma characterization is to understand, at a fundamental level, the nature of the turbulence and resulting cross-field transport. Not only does this impact the width of the scrape-off layer plasma, but it can also give rise to an edge transport barrier as in the H-mode transition for tokamaks. At the same time, the turbulence simulations need to begin with full edge-plasma profiles from two-point estimates, transport simulations, or experimental data. For the short term, turbulence simulations can give important information on the toroidal and poloidal distribution of power leaving the LCMS which can be used to improve the wall power-deposition calculations even using the field-line tracing models.

Progress has been made in adapting the BOUT turbulence code to stellarator geometry. BOUT has recently been generalized beyond the standard asymmetric tokamak geometry to accept any generalized magnetic coordinate configuration, including stellarators. Such calculation will give us a physics-based tool for setting the turbulent transport coefficients in the BoRiS transport code. Testing of this new version of the code is underway. An important issue for stellarators is the more rapid variation of the magnetic field strength along **B**, thereby requiring higher spatial resolution.

We plan to use the results of the turbulence modeling to determine the turbulence cross-field diffusion coefficients for use in the transport code and to learn how these scale with parameters and changes to the equilibrium. In the long term (several years), we envisage a more direct coupling between the turbulence and 3D transport simulations. In addition to giving a fundamental characterization of the scrape-off layer plasma, the turbulence calculations should give an understanding of possible core transport barriers in the stellarator edge; this is of major importance to any confinement device.

10.8. Plasma boundary diagnostics

In any experimental program, the list of proposed diagnostics contains those that are essential to the operation of the device, those that are highly desirable to obtaining the physics understanding required from the experimental program and more advanced diagnostics that give information on detailed physics issues. This situation is also true for the NCSX project. In addition, the construction and operation of NCSX as a new device is anticipated to occur in phases, each of which having a particular set of machine capabilities and physics objectives. The proposed boundary plasma diagnostics described below are organized first in terms of the phase of NCSX operation to which they would be applied and then categorized as essential, highly desirable or advanced.

Phase 1: Initial operation shakedown

The goal of this initial operation phase will be to produce the first plasma in the device. The objective as far as the boundary plasma is concerned will be to document the production of the plasma and to observe as much of the boundary plasma / material wall interaction as possible.

The essential boundary diagnostics in this phase are visible survey cameras. The goal of the cameras will be to document the production of the first plasma by recording images of light emitted from the SOL and to determine the locations of plasma wall interaction both toroidally and poloidally. This provides the basic feedback to initial attempts to position the plasma properly in the vacuum vessel. The survey cameras at this stage should have a tangential view so that as much of the toroidal extent of the plasma as possible can be documented. They should be spatially calibrated so that the precise location of image features that appear during the first plasma discharges can be determined. The camera systems should be outfitted with selectable neutral density attenuation filters so that the image intensity can be kept below saturation. Despite the complicated 3D geometry of NCSX a broad tangential view of the plasma should

provide valuable information to guide proper positioning of the initial plasma in the vacuum vessel.

Phase 2: Vacuum and field line mapping

The critical objectives of this phase as far as the plasma boundary is concerned are to verify the vacuum conditions, including an assessment of the initial wall conditions (outgassing, pumping, recycling, impurity generation), to validate the calculations of field line mapping, and to locate regions of excessive plasma wall interaction. There is no plasma operation planned for this phase.

The essential boundary diagnostics in this phase are the visible survey cameras and the vacuum system pressure and residual gas analyzer (RGA) gauges. The goal of the visible cameras is to determine the locations and characteristics of plasma wall interaction both toroidally and poloidally. This phase will be dominated by electron beam mapping of flux surfaces and attempts to predict regions of future plasma wall interaction. It may be possible to use the survey cameras to detect the locations of interaction of the electron beam with the plasma facing surfaces as an indication of the future strike points of the plasma on the wall. The pressure and RGA gauges will be used to detect the effect of various wall conditioning procedures on the quality of the vessel vacuum.

Phase 3: Ohmic Operation

The boundary plasma goals during this phase are to assess the effect of plasma wall interaction (both location and source rate) on core plasma performance, to achieve control of the plasma wall contact locations, and to begin the characterization of the SOL plasma.

The additional essential boundary diagnostics for this phase include line integrated visible filterscopes and near surface thermocouples in the target plates. Given success with optimizing the plasma positioning using the visible survey cameras, the target regions of interest should be the tips of the banana cross sections and the inner midplane of the bullet cross section where the limiters are. The boundary diagnostics should be concentrated in these regions.

The purpose of the filterscopes is to determine the source rate of recycled neutrals at critical locations. Therefore an array of filterscopes should view the tip of the banana cross section and another array should view the inner midplane of the bullet cross section. The filterscopes should be equipped with both D_alpha line filters so that the main ion recycling fluxes can be calculated, and also with filters for impurity lines such as CII (514 nm) and CIII (465 nm). Control of the production and transport of recycling neutrals will be the primary goal of the second generation of the PFCs. These will be installed in the tips of the banana cross section during the 5th phase of the project.

A first measurement of target plate heat flux is essential in this phase so that the power balance of 3D simulations can begin to be compared with experiment. These validated computer simulations are needed to guide the design of the 2nd generation PFCs to be installed in Phase 5. This first measurement can be done with an array of thermocouples mounted in the tiles of the

banana tip regions. Arrays should be mounted in both banana tips to check the symmetry of the heat flux between the future divertor regions.

Finally, highly desirable boundary diagnostics in this phase include IRTV cameras, Langmuir probe arrays (LPs) in the plasma wall contact region ("target plates") and a moveable probe of the SOL plasma especially in the banana tip regions. These diagnostics will provide, respectively, the target region heat flux profile with good spatial resolution, the target plate particle flux profile and samples of the spatial profiles of ne, Te and plasma flow velocity in the region where the optimized PFC hardware will be installed. In each case, the measurement contributes the detailed plasma characteristics needed to validate the computer simulations of the boundary plasma in the region where the new PFC hardware hopes to achieve power and particle control in Phase 5.

Phase 4: Auxiliary Heating

The goal of this phase as far as the boundary plasma is concerned is to re-characterize the SOL plasma in the presence of substantial auxiliary heating power. This includes determining the effect of heating power on wall conditions, evaluating the efficacy of wall coating techniques for improving wall conditions with heating power, and possibly examining the effect of biasing parts of the wall on the SOL performance and core confinement.

For this stage all of the essential diagnostics from the previous stages are needed and the three desirable diagnostics from the ohmic phase (IRTV cameras, LP arrays in the targets and a moveable probe) are now essential. The heating conditions during this phase will be close to those used with the 2nd generation PFCs (although the heating power will be somewhat lower) so complete measurements of the plasma conditions in the banana tips are required to complete the design of the new hardware.

The pressure of the neutral gas in both the banana tips and near the midplane of the bullet cross section should also be measured during this phase. This will require at least two ASDEX type pressure gauges with time response short compared with the plasma transitions induced by application of the auxiliary heating power. It would be desirable to have a third ASDEX gauge in the opposing banana tip region to check for up/down asymmetries.

To examine the effect of wall coating techniques on the boundary plasma the filterscopes and visible cameras should be upgraded to include imaging of some of the wall coating elements. Filters for visible lines of lithium (neutral and singly ionized) and boron should be available. If boronization is used then visible lines of helium should also be monitored since substantial helium is trapped in the boronization process and multiple discharges can be required after boronization to bring the helium concentration down to normal levels.

Finally, highly desirable boundary diagnostics in this phase include bolometer measurements, a visible survey spectrometer and a reciprocating probe of the SOL plasma especially in the banana tip regions. These diagnostics will provide, respectively, the total radiated power, the relative contributions to the radiated power from separate constituents of the SOL plasma (vis. deuterium neutrals, carbon species and other impurities), and detailed spatial profiles of ne, Te

and plasma flow velocity in the region where the optimized PFC hardware will be installed. In each case, the measurement contributes the detailed plasma characteristics needed to validate the computer simulations of the boundary plasma in the region where the new PFC hardware hopes to achieve power and particle control in Phase 5.

Phase 5: Confinement and Beta Push

At some point during this phase a new set of plasma facing components will be installed. The goal of the new PFCs will be to handle the high heat loads that result from substantial auxiliary heating of the core plasma and to control (minimize) the influx of recycling neutrals and sputtered impurities from the plasma targets back to the core plasma. This hardware will function much like a poloidal divertor in tokamaks including target surfaces optimized to handle high heat flux, baffle structures to restrict escape of neutrals from the divertor region back to the core, and possibly active pumping of neutrals to control the SOL and core plasma density. In addition, the potential for pumping of helium exhaust from the core will be examined in this phase by injecting trace levels of helium.

The list of essential diagnostics for this phase includes the divertor region bolometer arrays, the visible spectrometer measurement of the radiating constituents in the divertor plasma and the divertor reciprocating probe. The new diagnostics that are essential in this phase are: 1) Penning gauges in the divertor plenum and midplane, and 2) simultaneous measurements of D_alpha with either D_beta or D_gamma emission from the divertor region. The penning gauges will be used to determine the fractions of various neutral gases in the pumping plenum compared with the SOL. The ratio of these concentrations is the divertor enrichment. The enrichment of helium in the divertor is the critical parameter for assessment of future helium exhaust schemes in compact stellarators.

Simultaneous measurement of multiple deuterium emission lines in the divertor provides a technique to quantify the level of detachment of the divertor plasma from the target surfaces. The ratio of the emission intensities from the different lines changes substantially for a detached plasma (high density and ~ 1eV temperature) compared with an attached divertor plasma (moderate density and > 10 eV temperature). Experiments will be done during this phase to determine the available parameter regime for detached divertor operation of NCSX. For future high power compact stellarators, as in tokamaks, it is likely that the plasma will need to be detached from the target surfaces to reduce the target heat fluxes to acceptable levels.

During the detachment experiments in this phase it will be highly desirable to have increased spatial resolution in the divertor region of radiated power measurements, constituent line emission measurements, target probe data. These upgrades will resolve the strong gradients between the hot upstream SOL plasma and the detached plasma near the target surfaces. These requirements can be achieved simply by increasing the number of lines of sight of the existing bolometer arrays, filterscope arrays and target mounted Langmuir probe arrays in the divertor region.

It will also be highly desirable to have volumetric measurements of electron density and temperature and measurements of the UV emission from various constituents in the divertor.

Measurements of n_e and T_e within the plasma above the target surfaces can be done, albeit in a perturbative way, with the reciprocating probe passing through the plasma above the divertor target. However, it would be desirable to have a Thomson scattering system in one of the divertors with measurements at a number of locations vertically off of the divertor target to provide non-perturbative measurements of n_e and T_e in the attached and detached divertor plasma. The measurement of UV emission in the divertor is needed because these lines will contain the majority of the radiated power in the divertor during detached operation. A UV SPRED spectrometer with a wavelength range of 10 – 160 nm would provide the required data. It would also be desirable to install UV survey cameras with views of the divertor to provide the spatial profile of the emission lines containing the largest fraction of the divertor radiated power. Previous experience with tokamaks indicates the radiated power will likely be dominated by CIV (155nm) and L_alpha (121nm) emission, both of which can be imaged with MgF2 optical components, UV-to-visible conversion phosphors and standard visible cameras.

Phase 6: Long Pulse

The goal of this phase of NCSX operation is to extend the highest performance of the device to a fully relaxed current profile. As far as the boundary plasma this means that the goal is to reach steady conditions near the optimum for core performance and not produce any increasing impurity sources or damage of target surfaces during long high power discharges. A 3rd generation of the PFC hardware may be installed at some point during this phase. Optimization of this final PFC design will come from the measurements and validated code modeling done during Phases 4 and 5

The focus of the boundary diagnostics in this phase will be on the conditions of the target material as the discharge length increases. Since toroidal non-uniformity will be important in this phase, the number of IRTV systems viewing the targets should be increased to cover all the targets. Each target should also be equipped with Langmuir probes.

With steady long pulse conditions in this phase it may be possible to do detailed investigations of SOL and divertor flows. The advanced diagnostics for measuring plasma flow in the boundary either use charge exchange emission from diagnostic neutral beams or Laser Induced Fluorescence (LIF) of impurity ions in the boundary plasma. Both techniques are being developed for tokamaks at the present time. The optimum technique to use for NCSX will be determined after they have been tried on present devices.

10.9 Fast Particles Leaving the Confined Plasma Boundary

For the initial operation NCSX will be designed for up to 6 MW of beam power in the 40 to 50 keV energy range. These beams will be injected tangentially in both the co- and counter-directions. As discussed in Chapter 6, the non-zero departure from perfect symmetry in stellarators will lead to enhanced levels of beam ion losses above those present in an equivalent axi-symmetric tokamak. The loss patterns of beam ions on the vacuum chamber wall might require wall armor to handle the respective heat fluxes and to minimize the generation of impurities. Within the Monte Carlo slowing-down model, the exit locations, exit times, pitch angles and energies of the beam ions, leaving the outermost closed flux surface, are recorded.

Assuming that beam ions then move rapidly through the open outer flux region, the recorded parameters are used in estimating power loading patterns on the vacuum chamber walls.

Some of the characteristics of a slowing-down beam for the parameters $n(0) = 6 \times 10^{19}$ m^{-3}, $T_e(0) = T_i(0) = 2.4$ keV have been calculated for the PVR reference case. Since we don't expect major changes for the M45 configuration, we discuss this case in the following. As an example, Figure 10-24 shows a histogram of the energy distribution of the escaping beam ions injected with 40 keV energy.

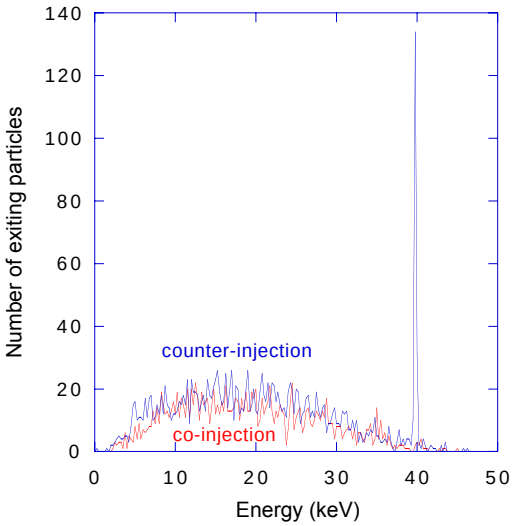

Figure 10-24. Energy spectrum of beam particles exiting the last closed magnetic surface

As can be seen, the energy losses are characterized by a broad distribution centered around 15 - 20 keV for both co- and counter- injection. The counter-injected ions also show a very sharp peak at the injection energy, presumably associated with prompt losses. It is important to know how much of the total injected energy is lost in fast particles, which is dependent on the injection energy. The result presented in Figure 10-24 has been based on 40 keV ion energy. The beams anticipated for NCSX will be capable of going up to 50 keV, but will also include lower energy components. In Figure 10-25 we investigate the variation of beam losses with injection energy as described above.

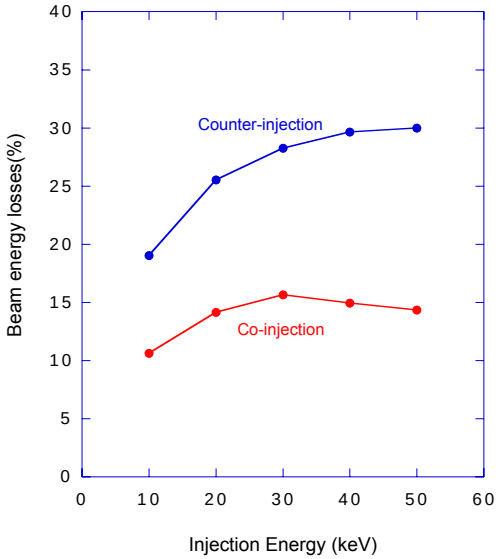

Figure 10-25. Variation of beam energy losses with injection energy for a machine design point at R_0 = 1.4 m, <B> = 1.23 T, n(0) = 8.5 x 10^{19} m^{-3}, $T_e(0) = T_i(0)$ = 1.58 keV

Based upon the current model, exit locations and energies are shown in Figure 10-5 for a typical case. Here the exit locations are plotted in Boozer poloidal and toroidal angle coordinates for the outermost flux surface. Colors are used to indicate the energy at which the fast ions leave the surface. As can be seen, most of the ions leave at intermediate energies from 10-20 keV, in similarity with Figure 10-26.

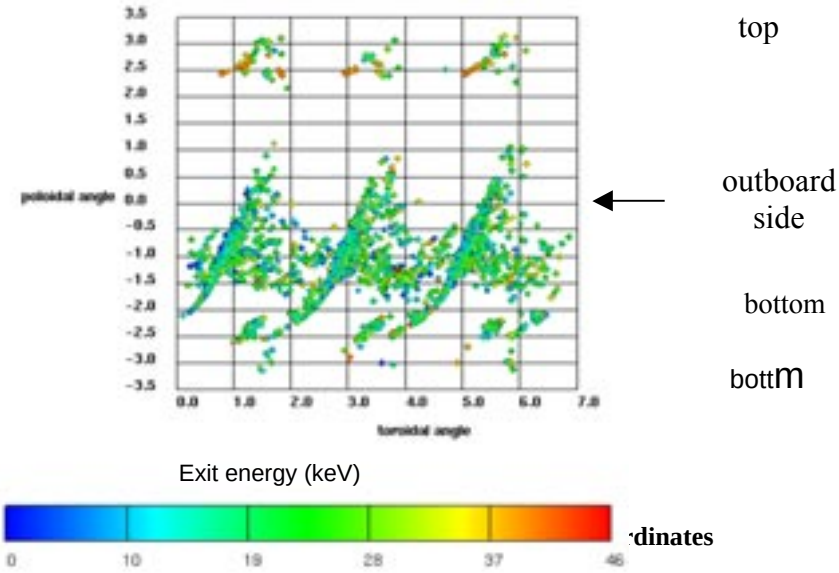

Figure 10-26. Loca dinates

The fast ion losses are primarily concentrated in helical stripes on the bottom of the vacuum vessel with one stripe per field period (shifting to the top with reversal of the magnetic field direction). We have also transformed this data into real-space coordinates. In Figure 10-27 we plot the data of Figure 10-26 vs. the normal cylindrical azimuthal coordinate, $\phi_{cylindrical}$ and a poloidal angle θ, which is equal to $\tan^{-1}[z/(R-R_0)]$.

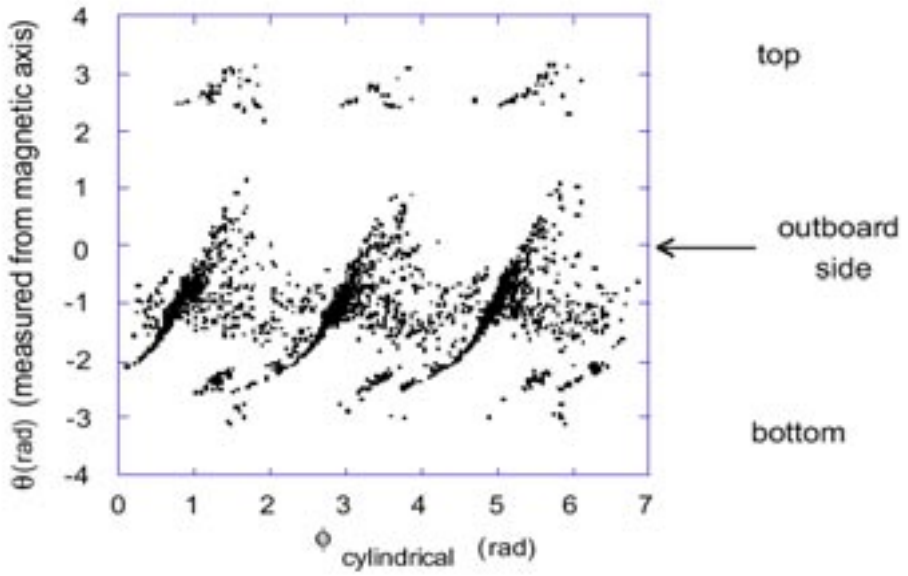

Figure 10-27. Location and energy spectrum of beam losses on outer surface in 2D Boozer coordinates

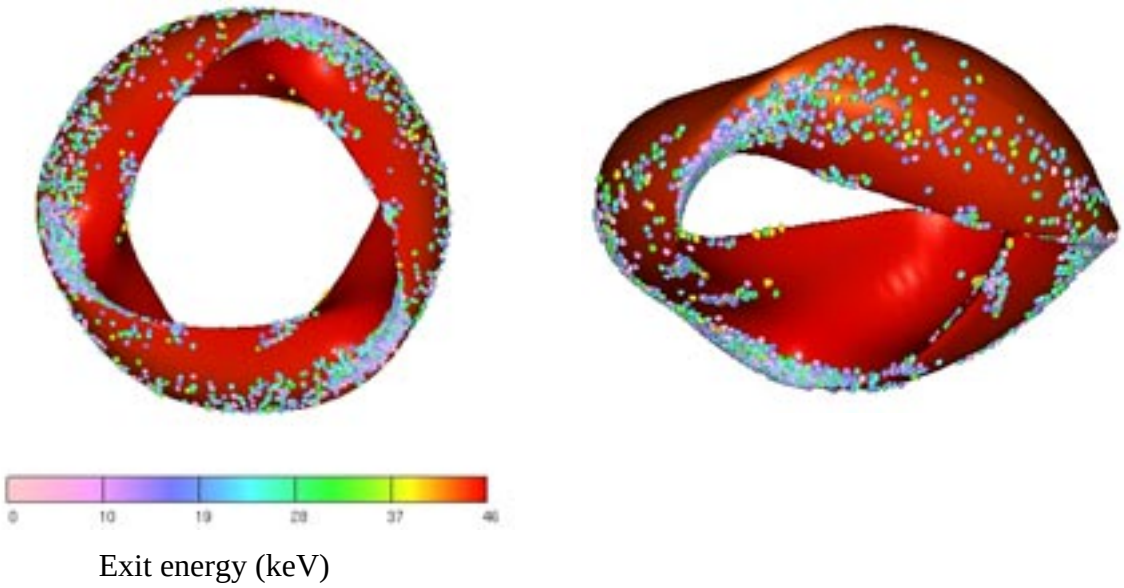

Figure 10-28. Location and energy distribution of beam losses on outer surface in 3D

Finally, we have plotted the ion loss locations on the three-dimensional outermost flux surface (Figure 10-28) as obtained from the VMEC stellarator equilibrium code. The flux surface is shown in red and the ion exit locations are color-coded according to the ion's energy at the time it passes through the flux surface. Again, it can be seen that the losses are somewhat concentrated, motivating the design of protective structures at these locations.

10.10 Vacuum Requirements and Wall Conditioning

10.10.1 Torus Vacuum Pumping Requirements

NCSX requires sufficient wall conditioning and pumping speed to achieve base pressures of at least 2-3 x 10^{-8} torr and to recover from discharges sufficiently to allow about a 5 minute discharge repetition rate. The legacy turbomolecular pumping system (TMP) from PBX-M consisting of four Leybold Heraeus, 1500 l/s pumps is available for NCSX. This pumping system, together with Ti gettering, was used on the unbakeable PDX, PBX, and PBX-M vessel to achieve base pressures of ~2-3 x10^{-8} torr and was able to recover vessel pressures from plasma discharges sufficiently rapidly to allow 3 to 5 minute discharge repetition rates, in spite of extensive internal hardware. The present plan is to mount a TMP on each of the high conductance NBI Transition Ducts, thus the application of this TMP system to NCSX will involve pump duct conductances comparable to or possibly greater than those encountered on PBX-M. In addition, if 100 Kl/s LHe Cryopumping capability is restored to the front end of each Neutral Beamline as planned, NCSX will have considerable extra pumping speed. After the initial pumping of atmospheric components is completed, the remaining partial pressure contributions will come mainly from H_2O, CO, CO_2 and hydrocarbons. The planned NCSX Bakeout, Glow Discharge Cleaning (GDC), and Boronization capability will greatly accelerate the cleanup of these impurities.

10.10.2 Vessel Bakeout

There is considerable agreement in the international fusion community regarding the desirability of baking fusion devices with graphite plasma facing components to about 350°C as the first step toward achieving optimum wall conditions. The physics basis for baking graphite to 350°C is discussed extensively in the ITER Report prepared from the draft titled "Considerations for Bakeout and Conditioning Specifications for In-vessel Components in ITER" prepared by D. Post, ITER JCT, Jan. 20, 1995 Revised May 2, 1995. This report lists the conditioning experience of major tokamaks. The final report was reviewed by the contributors from the major tokamaks. Their interesting verbatim comments/suggestions are given in the report and form a compendium of experience that will be adopted for NCSX wall conditioning.

10.10.3 Glow Discharge Cleaning

NSTX presently uses two fixed GDC anodes; other experiments (e.g., DIII-D, JT-60U) use 2 or more GDC anodes. Given uncertainties about GDC initiation and performance in the NCSX geometry, the Helium Glow Discharge Cleaning (HeGDC) design plans for 3 ports with 4.5 inch O.D. flanges equally spaced toroidally for fixed wall anodes. These anodes will be used for both GDC and gaseous boronization. The poloidal angle of these ports is not critical although symmetrical placement will facilitate monitoring and performance analysis. In addition to the anode ports, it is desirable to have 3 ports with 4.5 inch OD flanges located near to the anode ports (preferably within line-of-sight) for Pre-ionization Filaments to facilitate GDC breakdown at the actual operating pressure and voltage. On NSTX, Pre-ionization Filaments are used routinely to initiate HeGDC between discharges, and in conjunction with ECE, to initiate plasma discharges [18,19].

10.10.4 Boronization

The NCSX Boronization method should be sufficiently convenient and economical to be an operational tool that can be applied quickly and as often as required. It should also have minimal environmental, health, and safety impact when used in the NCSX Test Cell. The NCSX Boronization method could be able to use hydrogenated or deuterated boron compounds depending on subsequent plasma operations.

A suitable and effective candidate compound for NCSX boronization is Trimethylboron [$B(CH_3)_3$ or $B(CD_3)_3$] which is presently in use at PPPL on NSTX about every 3 weeks. Trimethylboron (TMB) is about a 1000 times less toxic than diborane and nonexplosive. TMB Boronization was first tested on TEXTOR where it was found to be comparable in effectiveness to Diborane and considerably safer [20]. In addition to TEXTOR, TMB Boronization has been applied extensively on COMPASS [21], Phaedrus [22], MAST [23], and NSTX [24].

The TMB Boronization procedure consists of using the regular NCSX Gas Injection and Torus Vacuum Pumping Systems. Using one Turbomolecular pump of the Torus Vacuum Pumping System, a standard HeGDC is applied for 10 min at about 4mTorr, ~450V, ~1A per each of 3 anodes. A mixture of 90% He and 10% TMB [$B(CH_3)_3$ or $B(CD_3)_3$] containing 10 grams of TMB is injected into the HeGDC until consumed (~160 minutes). This application is followed by a 2 hr HeGDC to remove the co-deposited hydrogen or deuterium from the ~ 100 nm, B/C film. In addition to the TEXTOR results which found TMB comparable to Diborane [20], work on Phaedrus with TMB [$B(CH_3)_3$], O-Carborane [$B_{10}C_2H_{12}$], and Decaborane [$B_{10}H_{14}$] found that core oxygen concentrations were lowest for TMB (B/C = 0.33). O-carborane (B/C = 5) had twice the oxygen as TMB and Decaborane (C = 0) had nearly 3 times the amount [22].

10.10.5 Lithiumization

Lithium wall conditioning is considered an attractive future upgrade of the NCSX wall conditioning system. Lithium pellet injection has been found to significantly improve TFTR plasma performance [25,26]. This involved using a Lithium Pellet Injector with a capacity of 270 pellets to inject up to four 3 mg lithium pellets per discharge at velocities of about 500 m/sec to near-core regions. A Lithium Pellet Injector will be a useful tool for initial NCSX lithium wall conditioning studies. However, this approach has both plasma and hardware limitations. Slow injection velocities are preferred because high injection velocities cause near-core deposition and perturbation. In addition, a small pellet size and a small number of pellets per injection may be required to prevent excessive perturbation of plasma conditions. Consequently, using lithium deposition via conventional pellet injection for plasma surface conditioning can require many discharges and is inefficient; however, other pellet injection methods might avoid these difficulties [27]. At this time, the optimum lithium characteristics have not been found, and little is known about the detailed plasma surface physics and chemistry of lithium deposited on graphite limiter surfaces [28]. The ability to increase the quantity of lithium deposition while minimizing perturbations to the plasma would provide NCSX with interesting experimental and operational options. Previous experience with Low Velocity Pellet Injection into discharges [27], Lithium Effusion Oven for deposition between discharges [29] and LASER induced ablation

during discharges [30] may be of interest to the NCSX Experimental Program. The planned port access will accommodate these options.

Finally, future upgrades to Li-based or other metal-based PFCs, building on the CDX-U and ALPS/APEX research, are considered.

References

[1] Grigull P. et al., EPS Conference, Madeira, Portugal, June 18-22, 2001
[2] Masuzaki S. et al., J. Nucl. Mater. 290-293 (2001) 17
[3] J. Nuehrenberg et al., IAEA Conference , Wuerzburg (1992) 449.
[4] Y. Feng et al., J. Nucl. Mater. 266-269 (1999) 812.
[5] R.W.T. Koenig, et al., 14th PSI Conference, Rosenheim, May 2000.
[6] E. Strumberger et al., Nucl Fusion, **37** (1997) 19.
[7] V.D. Shafranov, L.E. Zakharov, Nucl. Fusion **12** (1972) 599.
[8] M.F.A. Harrison et al., Nucl. Technol./Fusion, Vol. 3 (1983) 432
[9] P. C. Stangeby, "The plasma Boundary of Magnetic Fusion Devices", IoP Publishing, 2000
[10] T. W. Petrie et al., J. Nucl. Mater. 241-243 (1997) 639.
[11] A. Koniges et al., submitted to Nucl. Fusion
[12] E. Strumberger, Nucl. Fusion 32 (1992) 737
[13] E. Strumberger, Nucl. Fusion 36 (1996) 891
[14] E. Strumberger, Contrib. Plasma Physics 36 (1996) 171
[15] J. Kisslinger et al., 21st EPS, Montpellier, 1994, 18B,I, 368
[16] J. Kisslinger et al., 22nd EPS, Bournemouth, 1995, 19C, III, 149
[17] K. McCormick et al., Proc. 12th Int. Stellarator Conference, Madison 1999.
[18] "NSTX Filament Preionization And Glow Discharge Cleaning Systems", H. W. Kugel, et al., PPPL Report-3381, November 1999, Proc. of the 18th Symposium On Fusion Engineering, Albuquerque, NM, October 25-29, 1999 (IEEE,1999) 296.
[19] "Overview of Impurity Control and Wall Conditioning in NSTX", H. W. Kugel, et al., Proc. of the 14th Int. Conf. on Plasma Surface Interactions In Controlled Fusion Devices, May 22-26, 2000. (To be published in J. Nucl. Mtrl.)
[20] "Borontrimethyl $B(CH_3)_3$ - A Less Hazardous Substance for Boronization", J. Winter, et. al. J. Nucl. Mater. 176 &177 (1990) 486.
[21] "Boronization of Compass", H. G. Esser et al, J. Nucl. Mater., **186** (1992) 217.
[22] "Boronization Effects on Phaedrus-T Rf Operation", M. Doczy, et al., Bull. Am. Phys. Soc. **39** (7) (1994) 1631.
[23] Private Communication, S. Fielding, Culham Science Centre, May 2000.
[24] "Intial Boronization of NSTX and the Effect On Plasma Performance", H. W. Kugel, et al., Bull. Am. Phys. Soc. **45** (7) (2000) 251.
[25] D. K. Mansfield, *et al*., "Enhancement of Tokamak Fusion Test Reactor Performance by Lithium Conditioning", *Phys. Plasmas* **3**, 1892 (1996).
[26] J. A. Snipes, *et al*., "Wall Conditioning With Impurity Pellet Injection on TFTR", *J. Nucl. Mater*., 196-198 (1992) 686.
[27] H. W. Kugel, et al., "Low Velocity Boron Micro-Pellet Injector For Edge And Core Impurity Transport Measurements", Unviersity, PPPL Report No. PPPL-3306, July

1998, Proceedings of 12th Topical Conference on High-Temperature Plasma Diagnostics, Princeton, NJ, June 7-11, 1998, Rev. Sci. Instrumen. **70** (1) (1999) 493.

[28] J. Hogan, C. Bush, and C.H. Skinner, "Lithium Effects In Plasmas, Summary Of The Workshop, PPPL, 17-18 October 1996"

[29] H. W. Kugel, et al., "Development of Lithium Deposition Techniques for TFTR", PPPL-3270, October 1997, Proceedings of 17th IEEE/NPSS Symposium on Fusion Engineering, 6-10 October, 1997, San Diego CA.

[30] D. K. Mansfield, et al., "DOLLOP: Improved Plasma Performance Using a New Concept for Mitigating the Plasma-Wall Interaction in Fusion Devices", Bull. Am. Phys. Soc. **42**(10) (1997) 1972, and D. K. Mansfield et al., "Observations Concerning the Injection of a Lithium Aersol into the Edge of TFTR Discharges", submitted to Nucl. Fus.